energies

MDPI

Article

Enhanced Quasi-One-Dimensional Modeling and Design Performance Assessment of an ORC with Radial Turbine for Waste Heat Recovery

Raffaele Carandente, Alessandro di Gaeta, Veniero Giglio and Fabrizio Reale *

Institute of Sciences and Technologies for Sustainable Energy and Mobility (STEMS-CNR), 80125 Naples, Italy; raffaele.carandente@stems.cnr.it (R.C.); alessandro.digaeta@cnr.it (A.d.G.); veniero.giglio@stems.cnr.it (V.G.)
* Correspondence: fabrizio.reale@cnr.it

Abstract

Organic Rankine Cycles (ORCs) are widely recognized as an effective solution for waste heat recovery (WHR). However, the design and optimization of these systems must address the tradeoff between computational efficiency and the need to capture complex component behavior. This requires moving beyond purely energetic 0D modeling approaches to account for constructional, spatial, and operational constraints. This work presents a novel modeling framework with a specific focus on the expansion device. Radial inflow turbine stages are selected for their capability to achieve high pressure ratios while maintaining compactness and high efficiency. Heat exchangers follow a generic one-dimensional counterflow configuration, with a shell-and-tube geometry adopted for sizing purposes. The turbine stages are modeled by resolving several internal sections in order to capture local thermofluid dynamic conditions. The framework predicts turbine efficiency and incorporates a newly developed formulation for shock-induced losses, improving performance prediction under trans-sonic flow conditions. After validation against experimental data, the model is applied to a WHR system integrated with an internal combustion engine fueled by biofuels. The results highlight the existence of optimal operating conditions arising from competing physical mechanisms. The analysis also shows the transition from single-stage to two-stage turbine configurations at high pressure ratios and emphasizes the role of real gas effects in determining stage performance and optimal expansion distribution. The results of simulations carried out for three different working fluids (ethanol, toluene, and R1234ze(E)) highlight that the available mechanical power ranges from 10 to 22 kW for single-stage turbine configurations and from 24 to 36 kW for two-stage configurations, with total system volumes varying between approximately 600 and 9000 L. Among the working fluids considered here, ethanol provides the best overall performance for the present case study. Overall, the proposed approach provides a reliable and computationally efficient tool for the preliminary design and optimization of ORC-based WHR systems.

Keywords: Organic Rankine Cycle; waste heat recovery; radial inflow turbine; shell-and-tube heat exchanger; loss model; ethanol

Check for updates

Academic Editor: George Kosmadakis

Received: 2 April 2026
Revised: 15 April 2026
Accepted: 18 April 2026
Published: 23 April 2026

Copyright: © 2026 by the authors. Licensee MDPI, Basel, Switzerland. This article is an open access article distributed under the terms and conditions of the Creative Commons Attribution (CC BY) license.

1. Introduction

Waste heat recovery is one of the most viable and promising approaches for increasing the net power output of energy systems without requiring additional primary energy input, and is used in both the industrial and transportation sectors [1]. Theoretically, the global

WHR potential is estimated to range between 5 and 15% of the primary energy input [2]. The integration of different thermodynamic cycles in combined-cycle configurations has long been widely adopted in both new installations and repowering applications, particularly through steam Rankine and Brayton cycles, allowing very high efficiency levels to be achieved. Increasing attention has been given to the adoption of WHR systems in medium- and small-scale plants, with emerging solutions including Organic Rankine Cycles (ORCs). ORC systems are considered suitable for recovering low- to medium-temperature waste heat thanks to their high flexibility, safety, and low maintenance requirements [3].

The selection of the working fluid is a crucial step in the proper design of an ORC system, and depends on several factors. Environmental sustainability has become a key requirement, particularly in terms of very low Ozone Depletion Potential (ODP) and Global Warming Potential (GWP). This aspect is especially relevant because several classes of organic fluids are being phased out under national regulations due to their unsatisfactory ODP and GWP [4]. A suitable working fluid should also be readily available, cost-effective, and exhibit favorable thermodynamic properties along with acceptable safety characteristics. On this point, Amicabile et al. [5] proposed the definition of a safety parameter based on information from the US System for the Identification of the Hazard Materials (NFPA 704) standard and fixing an upper limit of this parameter at two. Several layouts can be considered to reach a good compromise between increased complexity and improved efficiency [6].

The potential of ORC systems combined with Internal Combustion Engines (ICEs) for waste heat recovery has been investigated since the early 1970s [7]. However, the proportion of research articles focusing on experimental campaigns and prototypes accounts for only about 10–12% of the total published literature [8], highlighting a predominant interest in numerical modeling of ORC systems. In this context, numerous studies have addressed off-design simulations under both steady-state and unsteady operating conditions [9]. In particular, with the regard to small-scale ORC systems, Moradi et al. [10] reviewed various modeling approaches for both the overall system and its components. These can be simulated using a variety of models, including deterministic [11], CFD [12], empirical, semi-empirical [9], polynomial regression [13], or single coefficients [14].

In small-scale applications, the choice of expander is often addressed toward scroll expanders, which are more widely adopted than other solutions [15]. Nevertheless, several studies have addressed the use of radial turbines in ORC applications. A simplified numerical approach treats expanders, particularly turbines, as black boxes by assigning a fixed isentropic or polytropic efficiency [16]. The use of characteristic operating maps based on corrected or reduced mass flows and rotational speeds, expansion ratio, and isentropic efficiency represents a widely adopted approach in steady state off-design and partial load analyses [17]. Wang et al. [18] reviewed and compared several loss models for the preliminary design of small-scale Radial Inflow (RIT), Radial Outflow (ROT), and Axial Turbines (AT) for ORC applications, with particular emphasis on small-scale systems. They concluded that RITs are recommended for medium and small ORCs with an expansion pressure ratio lower than 10. In addition, they stated the typical operative ranges of RITs are 9.3–684 kW and 3000–114,000 rpm, with efficiency between 56.1 and 91.75%. In particular, the simplest approach estimates flow loss using a friction model [19]. Meroni et al. [20] based their loss model mainly on the equations of the Baines model [21], which primarily consists of incidence loss, passage loss, tip clearance loss, and windage loss. The model proposed by Fiaschi et al. [22] is mainly related to the Rodgers model [23], which estimates flow loss according to the turbine geometry and operational condition. Erbas and Biyikoglu [24] modeled losses using the Baines model and the Wasserbauer and Glassman model [25]. Moreover, two-stage radial inflow turbines can increase the usual expansion ratio adopted for ORC plants [26,27].

One of the most interesting applications at medium to small scales concerns the integration of an Internal Combustion Engine (ICE) with an ORC system. Over the last two decades, this solution has attracted increasing interest [28,29].

Shi et al. [30] reviewed various ICE-ORC solutions, starting from the consideration that the specific TS shape of the ideal cycle for ICE-WHR systems resembles a triangle. This differs from the shape of other WHR fields due to the large temperature gradients typical of this integration. The use of alkanes, aromatics, siloxanes, and alcohols enables the development of High-Temperature ORC (HT-ORC) systems. As highlighted by Shi et al., superheating is not necessary when dry or isentropic fluids are employed, as this approach prevents impingement of liquid droplets on the expander blades; for wet fluids, superheating remains necessary. Shi et al. reviewed several HT-ORC systems coupled with ICEs, mainly operating in subcritical conditions but also considering transcritical configurations.

Shu et al. [31] proposed a simple subcritical ORC system at the bottom of a six-cylinder, four-stroke supercharged diesel generator able to provide 235.8 kW under rated conditions, with torque of 1500 Nm. The design of the turbine was addressed using the Volumetric Flow Ratio (VFR) and a related size parameter. The model was built in Matlab and based on the first and second laws of thermodynamic using REFPROP [32] for the real working fluid properties. The authors carried out both energetic and exergetic analysis. The results of their simulations highlighted that working fluids with a higher number of carbon atoms in the chain had higher thermal efficiency and that molecular complexity had a significant and positive impact on both SP and VFR.

Kolsch et al. [33] studied a WHR system located at the exhausts of a six-cylinder four-stroke diesel engine with 235.8 kW of available power and torque of 1500 Nm. The authors considered three different working fluids (methanol, toluene, and Solkatherm SES36) in steady-state operating conditions. The isentropic efficiencies of pump and turbine were fixed at 0.8 and 0.7, respectively, with REFPROP used for the fluid properties. The evaporator was modeled considering Chen correlation integrated with Forster and Zuber correlation. The results of numerical simulations highlighted that although toluene presented the highest net power output, methanol as better suited due to its ORC being more stable and providing higher average thermal efficiency.

Fatigati et al. [34] developed a dynamic model of an ORC unit installed at the exhaust of a 3.1 L turbocharged Diesel engine using GT-Suite, combining 0D and 1D thermofluid dynamics approaches. The pump and expander were modeled as 0D components, while the heat exchangers were described using a master–slave scheme. For the working fluid (R245fa), heat transfer coefficients were evaluated using the Colburn correlation in single-phase conditions, Plate et al. during condensation, Plate and Kandlikar during evaporation, and Dittus–Boelter in supercritical conditions. The system dynamics were simplified by considering only the HRVG transient behavior in order to preserve physical consistency. A second lower-cost dynamic model based on a Permeability–Moving Boundary (P-MB) approach was also developed. Validation against experimental data showed errors of 4–7% for the GT-Suite model and above 10% for the P-MB model. In a subsequent study [35] the same authors investigated control strategies, proposing a feedforward–feedback control system for ORC units coupled with ICEs.

Giglio et al. [27] modeled a full ethanol ICE-ORC system for EV charging stations, using GT-Suite for an 8.7 L turbocharged E100 engine and Thermoflex for a two-stage radial turbine ORC with ethanol as the working fluid. A preliminary analysis identified the optimal expansion ratios, while the 0D thermodynamic model was performed assuming fixed efficiencies and losses. Results showed that the two-stage configuration improved overall mechanical efficiency and available power up to 12.8%.

Wei et al. [36] proposed two alternative approaches for a dynamic model of an ORC. The model was built in Modelica language, simulated with Dymola, and validated against experimental data. The evaporator and condenser were discretized in five cells. Regarding the heat transfer correlation, the Gnielinski equation was used for single-phase fluid, while a correlation from Värme Atlas was used for two-phase flows in horizontal tubes. Pressure losses were taken into account. The pump was empirically modeled using performance data provided by the manufacturer, while the turbine was modeled using a map.

Despite the extensive research on ORC systems, most existing models rely on simplified 0D component representations, which often neglect important phenomena related to the interaction between local fluid dynamics and component geometry. The present work addresses this limitation by proposing a modeling framework that integrates a detailed analysis of the Radial Inflow Turbine (RIT) stages with a standard 1D approach for the Heat Exchangers (HX). In particular, the turbine model is referred to as quasi-1D, since it resolves the flow across several intermediate physically relevant sections rather than considering only the inlet and outlet states. This focus on internal flow properties is combined with a comprehensive treatment of turbine losses, including a newly developed formulation for shock-related losses, to enable realistic predictions of turbine efficiency and stage sizing. The heat exchanger models account for practical operating effects such as pinch-point temperature differences, pressure drops, and the influence of flow characteristics on heat transfer coefficients. The proposed framework maintains the computational efficiency required for system-level optimization while capturing both energy performance and layout limitations.

The main original contribution of the present work lies in its integration of different component and sub-component models into a unified quasi-1D system-level tool, including decisions about which physical phenomena to retain and which to simplify as well as the way in which these are coupled together. At the component level, the proposed shock loss model for the radial inflow turbine represents the main individual contribution, while the selection and combination of loss models from the literature into a coherent framework while carefully avoiding overlapping mechanisms and gaps in the loss breakdown likewise constitutes an original element of the work.

The rest of this paper is organized as follows: Section 2 presents the modeling framework and its validation against experimental data; Section 3 reports the main results obtained for a waste heat recovery system applied to an ICE fueled with bio-ethanol, analyzing the impact of key design variables on overall system performance; finally, Section 4 summarizes the main findings and contributions of the work.

2. ORC System Modeling and Validation

The proposed framework adopts a component-based architecture in which each element, including the pump, the turbine, and heat exchanger, is modeled independently through its own set of governing equations. The flow is resolved at several key locations within the components. Closure of the thermofluid dynamic problem is performed by solving the Helmholtz equation of state embedded in Coolprop [37], including determination of any point of interest (both static and stagnation thermodynamics) described by pressure (p), temperature (T), density (ρ), enthalpy (h), entropy (s), and vapor quality (Q). It also calculates flow velocity (c) and flow angles (α absolute, β relative) as well as relevant thermophysical properties such as dynamic viscosity (μ), thermal conductivity (k), speed of sound (a), surface tension (σ), isothermal compressibility, isobaric compressibility, and specific heat capacities (c_p, c_v). These properties are treated as area-averaged quantities. Although some studies have applied a blockage factor to account for boundary layer effects, such correction is not adopted here because the velocities already represent

section-averaged values. These local quantities form the basis for the detailed analysis and sizing of each component.

Within this architecture, the radial inflow turbine stages follow a mean line representation that combines conservation equations with semi-empirical correlations to account for losses and flow related phenomena that would not be captured by purely 0D or 1D formulations. Specifically, this work introduces an original model for shock-induced losses, which is particularly relevant for turbines operating at high expansion ratios where supersonic conditions at the nozzle exit are frequently encountered. Other loss contributions are incorporated through a curated selection of literature-based methods. Although combining empirical approaches from different authors can introduce challenges due to differing assumptions, the current selection ensures a comprehensive description of the main loss phenomena while strictly avoiding overlapping mechanisms. Moreover, these models are adapted where necessary to account for the non-ideal behavior of the working fluids compared to the ideal gas assumption.

Similarly, the heat exchanger model relies on first principles and semi-empirical formulations that leverage the above-mentioned thermofluid dynamic properties to determine relevant quantities such as temperature profiles, heat transfer coefficients, and total pressure drops. Compressors, pumps, and other auxiliaries are modeled in a simplified manner.

The integration of these component models allows the framework to provide a complete description of the WHR system, including its interaction with the heat source, which in this case is a biofueled ICE.

2.1. Radial Inflow Turbine

The radial inflow turbine model solves the flows and computes the passage areas at all stations shown in Figure 1, including the intermediate nozzle sections t and g.

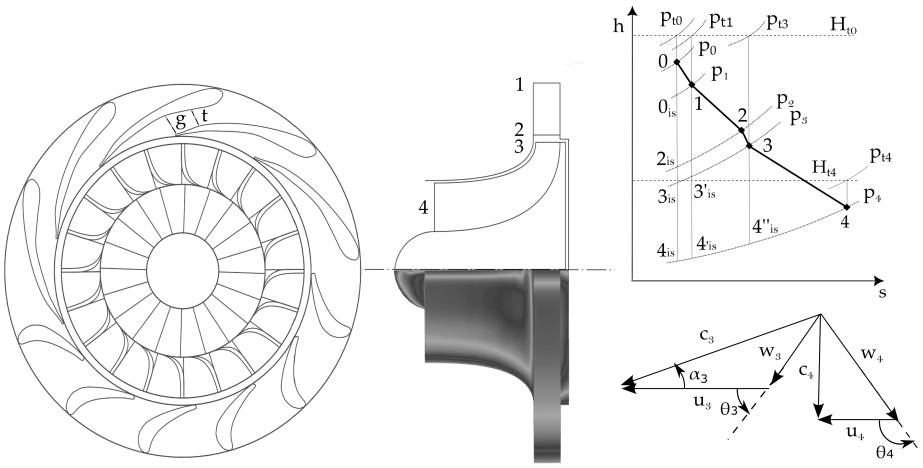


Figure 1. Radial inflow turbine: frontal view (**left**), meridional view (**middle**), and HS plane with velocity triangles (**right**). The stations are labeled as: 0 (volute inlet), 1 (volute outlet/stator inlet), 2 (stator outlet), 3 (rotor inlet), and 4 (rotor outlet). The intermediate nozzle sections are denoted by (t) and (g).

Figure 1 illustrates the schematics for both a convergent–divergent nozzle for use when supersonic conditions develop within the nozzle ($M_2 > 1$) and a purely convergent nozzle for subsonic flow at the stator exit ($M_2 < 1$). In the latter case, sections g and t coincide; furthermore, it is assumed that the passage width b remains constant from the volute exit to the rotor inlet, i.e., $b_1 = b_2 = b_3$.

The non-dimensional relations presented below stem from the rotor angular momentum equation, and can be formulated in terms of either absolute or relative flow quantities. These relations provide the isentropic flow angles as functions of the design input parameters (Table 1).

$$\psi_{is} = \phi_{is}\left[\cot\alpha_{3is} - \frac{MVR_{is}}{X_r}\cot\alpha_{4is}\right] \approx \phi_{is}\cot\alpha_{3is} \tag{1}$$

$$\psi_{is} = 1 + \phi_{is}\left[\cot\theta_{3is} - \frac{MVR_{is}}{X_r}\cot\alpha_{4is}\right] \approx 1 + \phi_{is}\cot\theta_{3is} \tag{2}$$

$$\cot\theta_{4is} = \cot\alpha_{4is} + \frac{1}{\phi_{is}}\frac{X_r}{MVR_{is}} \approx \frac{1}{\phi_{is}}\frac{X_r}{MVR_{is}} \tag{3}$$

As is well known in turbomachinery theory, the maximum work extraction condition corresponds to $\alpha_4 = 90°$, which also implies $\alpha_{4is} \approx 90°$. The approximate forms of Equations (1)–(3) refer specifically to this condition, which is also adopted for the design investigation relative to the case studies presented in the next section.

Table 1. Summary of inputs to the radial turbine design model.

Category	Description	Definition
Requirements	$\dot{m}$	Mass flow rate.
	β_{tt}	Total-to-total pressure ratio (P_{t0}/P_{t4}).
Inlet boundary conditions	P_{t0}	Total pressure at the turbine inlet.
	T_{t0}	Total temperature at the turbine inlet.
Design Variables	M_0	Mach number at the turbine inlet.
	ψ_{is}	Isentropic work coefficient ($\Delta H_{t,is}/u_3^2$).
	ϕ_{is}	Isentropic flow coefficient ($c_{3is,m}/u_3$).
	b_3^*	Non-dimensional channel width at rotor inlet (b_3/D_3).
	MVR_{is}	Isentropic rotor meridional velocities ratio ($c_{4is,m}/c_{3is,m}$).
	X_r	Rotor diameter ratio ($D_3/D_{4,m}$).
	X_v	Volute diameter ratio (D_0/D_1).
	AR_v	Volute aspect ratio.
	$\alpha_{4,is}$	Absolute rotor outlet flow angle (isentropic).
	$l_{z,r}^*$	Non-dimensional rotor axial length ($l_{z,r}/D_3$).
	ϵ_i^*	Non-dimensional nozzle–rotor radial gap (ϵ_i/D_3).
	ϵ_r^*	Non-dimensional rotor tip clearance (ϵ_r/D_3).
	ϵ_b^*	Non-dimensional rotor–backplate axial gap (ϵ_b/D_3).
	$t_{te,n}^*$	Non-dimensional nozzle trailing edge thickness ($t_{te,n}/o_2$).

A flowchart overview of the in-house developed turbine design procedure is shown in Figure 2. The scheme includes dedicated sub-procedures for the analysis of key inter-blade control volumes, which are necessary to resolve nozzle flow deviation, determine the main blade geometric parameters such as nozzle blade angles and preliminary profiles, and estimate the various loss contributions.

In particular, a control volume approach is applied between sections g and 2 of the nozzle using geometrical relationships, mass continuity, and the momentum equation in the direction perpendicular to section g. This method provides the nozzle deviation angle

δ_n, nozzle exit blade angle $\alpha_g = \alpha_{2,b}$, opening o_g, and flow properties at section g according to the following equation:

$$\frac{\tan(\delta_n + \varphi)}{\tan(\alpha_g - \varphi)} = \frac{\rho_g}{\rho_2}\frac{\sin\varphi}{\varphi}\frac{\sin(\alpha_g - \varphi)}{\left[1 + \frac{1}{\gamma_{pv,g}\, M_g^{*2}}\left(1 - \frac{\sin(\alpha_g - \varphi)}{H}\cdot\frac{p_2}{p_g}\right)\right]} - 1 \quad (4)$$

where φ is the angular spacing defined by two consecutive blades, i.e., $\varphi = 2\pi/Z$, H is a geometric term depending on φ,α_g, and the nozzle's trailing edge thickness to pitch ratio $t^*_{te,n}$. The quantity $M^*_g = \sqrt{\gamma_{pv,g}\, R\, Z_g\, T_g}$ provides a reliable approximation of the Mach number for real gases [38], with γ_{pv} denoting the isentropic pressure–volume exponent for a real gas. Equation (4) is solved iteratively to determine the quantities described above, since it depends implicitly on α_g. Moreover, this formulation implicitly accounts for losses originating in the last nozzle segment between sections g and 2. Among these loss sources, the shock system forming at the nozzle exit (see Figure 3) has the most significant impact on the flow deviation, turning the flow to varying degrees and causing departures from the ideal direction defined by the blade geometry.

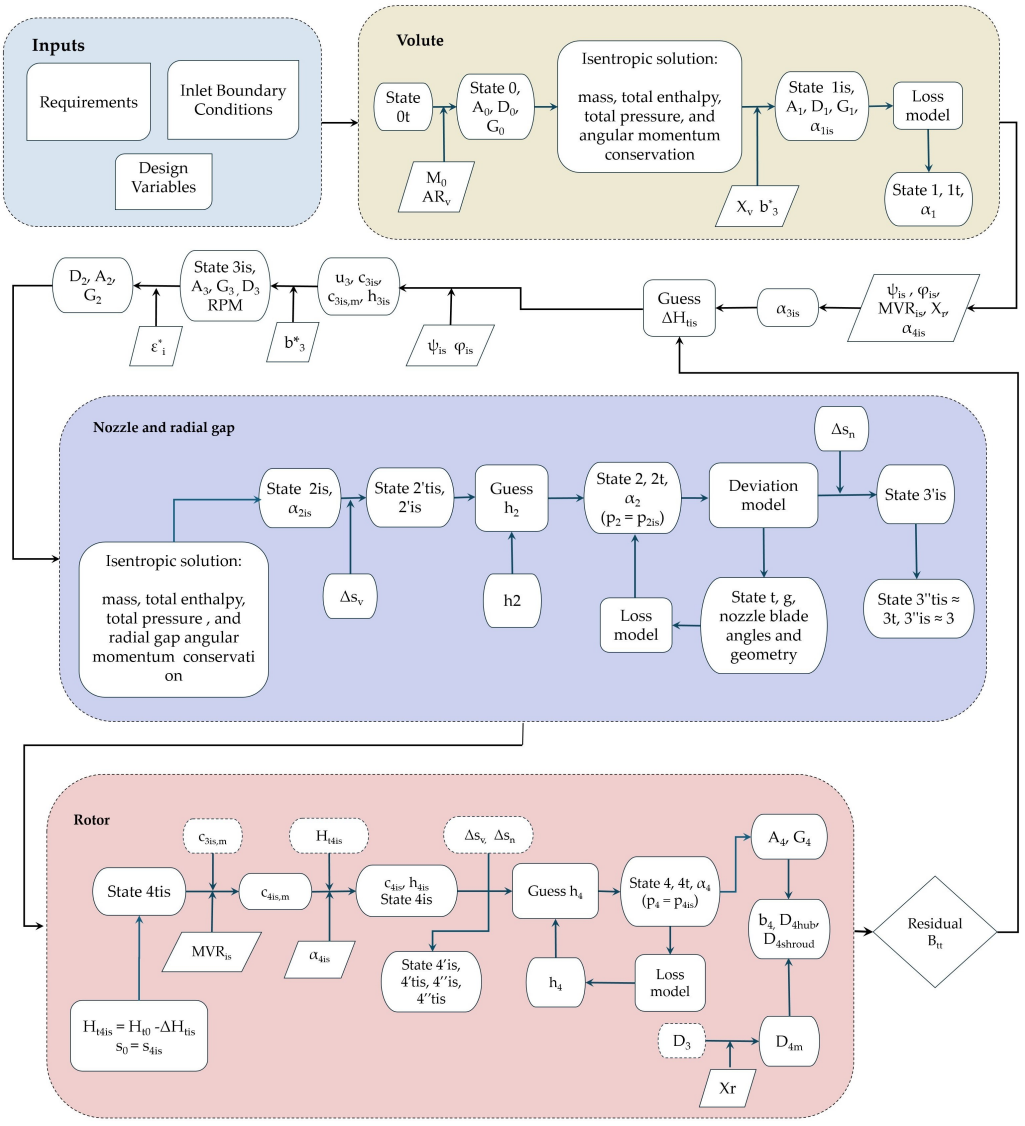


Figure 2. Outline of the design procedure for a radial inflow ORC turbine.

The loss model accounts for contributions from the volute, nozzle, and rotor; for simplicity, the radial gap between the nozzle and rotor is assumed to behave isentropically (see Figure 1, right). The corresponding expressions for entropy and enthalpy losses are

$$\Delta s = \Delta s_{\mathrm{v}} + \Delta s_{\mathrm{n}} + \Delta s_{\mathrm{r}} = (s_1 - s_0) + (s_2 - s_1) + (s_3 - s_2), \tag{5}$$

$$\Delta h_{\mathrm{loss}} = \Delta h_{\mathrm{loss,v}} + \Delta h_{\mathrm{loss,n}} + \Delta h_{\mathrm{loss,r}} = (h_1 - h_{1\mathrm{is}}) + (h_2 - h'_{2\mathrm{is}}) + (h_4 - h''_{4\mathrm{is}}). \tag{6}$$

The above loss definitions define both the total-to-total and total-to-static turbine stage efficiencies:

$$\eta_{tt} = \frac{H_{t0} - H_{t4}}{H_{t0} - H_{t4,\mathrm{is}}}, \qquad \eta_{ts} = \frac{H_{t0} - H_4}{H_{t0} - h_{4,\mathrm{is}}}. \tag{7}$$

Each term in Equation (6) arises from multiple loss mechanisms, as summarized in Table 2. Volute friction and stator profile losses calculation follows the method proposed by Aungier [39], derived from boundary layer theory and applied in previous studies (e.g., Da Lio [40]). Secondary losses, sometimes referred to as endwall losses, result from 3D flow phenomena such as passage vortices near the hub and blade surfaces. For the nozzle, this energy dissipation is quantified using the model by Benner et al. [41]. Mixing losses account for the dissipation associated with the homogenization of non-uniform flow conditions downstream of the blade trailing edges. For this contribution, the original model proposed by Denton [42] requires evaluation of the base pressure [43]. We extend Denton's model by introducing the effective base pressure coefficient proposed by Baumgartner et al. [44] and recommended by Majer and Pini [45]. This correction accounts for compressibility effects and the non-ideal behavior of dense vapor flows through use of the pressure–volume isentropic exponent γ_{pv}. Evaluation of rotor losses is based on the work of Baines [46,47], providing a unified formulation for losses through the blade passage, complemented by tip-clearance losses. Disk friction losses are mainly due to viscous interaction between the rotor and the fluid in the gap between the rotor and the backplate. Following Ventura [48], these losses are calculated using the Daily and Neece model [49], with the loss in terms of Δh computed according to Ghosh et al. [50].

Table 2. Summary of the empirical models adopted in the present work.

Component	Item	Models
Volute	Friction losses	Aungier [39].
Nozzle	Profile losses	Aungier [39].
	Secondary losses	Benner et al. [41].
	Mixing losses	Denton [42] with correction for non-ideal flows from Baumgartner et al. [44].
	Shock losses	Dedicated model developed in the present study.
	Blade number	Zweifel [51].
Rotor	Passage losses	Baines [46].
	Tip clearance losses	Baines [46].
	Disk friction losses	Daily and Neece [49].
	Blade number	Glassman [52].

Incidence losses are not considered in this study, as they occur only under off-design conditions. Finally, the so-called "kinetic energy loss" corresponding to the specific kinetic energy at the rotor exit is included in the calculation of the total-to-static efficiency.

The loss estimation ends with the shock loss model, which aims at the capture of dominant phenomena under trans-sonic and high pressure ratio conditions. In the present context, the term *transonic* refers to a flow regime in which the fluid enters the nozzle

passage under subsonic conditions, reaches the sonic state at the throat section, and subsequently undergoes a supersonic expansion along the divergent portion of the blade channel. Figure 3 shows the typical shock pattern forming at the trailing edge of a supersonic exit turbine vane [43,53,54] when operating under design conditions. With reference to design working conditions, the underlying assumption is that the divergent section of the blade passage is properly designed, for instance using the method of characteristics [55,56], such that no additional shock systems are generated within the channel. In contrast, the shock system shown in Figure 3 is inherent to the flow and not a consequence of poor design, as it is intrinsically associated with the curvature of the blade's trailing edge. This curvature induces a rapid turning of the supersonic flow, which for a flow exhibiting ideal gas dynamic behavior results in an expansion fan, as shown in the detail of the trailing edge flow in Figure 3. This local overexpansion is subsequently corrected by a shock system that restores the imposed downstream static pressure.

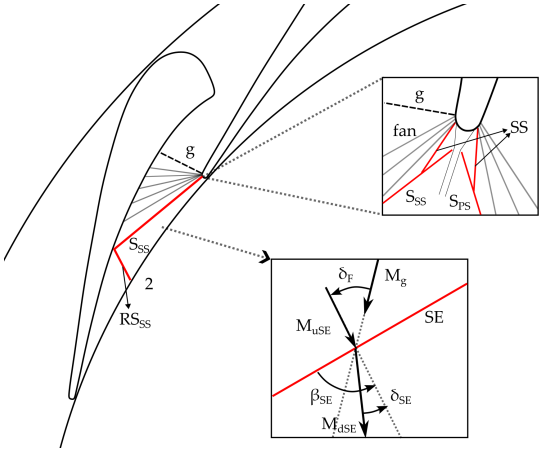


Figure 3. Typical shock pattern at the trailing edge of a supersonic turbine vane. Station 2 denotes the vane outlet section.

In contrast, certain fluids, known as Bethe–Zel'dovich–Thompson (BZT) fluids [57], may reach thermodynamic states for which the fundamental derivative of gas dynamics Γ [58] becomes negative. When $\Gamma < 0$, the flow exhibits non-classical gas dynamic behavior that is completely opposite to that observed in ideal gases. In particular, theory predicts the occurrence of supersonic flow fields featuring compression rarefaction waves and expansion shocks [59]. More recently, these phenomena have also been observed experimentally [60]. In a turbine cascade, a flow operating in this thermodynamic regime generates a compression fan at the nozzle trailing edge as a consequence of the local curvature, followed by a system of expansion shocks that adjusts the flow to the downstream imposed static pressure [61]. The present model is generalized with respect to the thermodynamic and gas dynamic behavior of the working fluid, accounting for ideal gas-like states, dense vapor conditions, and supercritical flows; however, a complete picture of all possible flow patterns requires further investigation. This aspect becomes especially relevant for machines operating under off-design conditions, where shock structures may differ from those discussed in the present work. The proposed model reduces the shock system shown in the figure, consisting of the separation shocks at the trailing edge (SS), the suction-side trailing-edge shock (S_{SS}), and the reflected suction-side trailing-edge shock (RS_{SS}), to a single equivalent shock (SE). This equivalent representation accounts for the overall shock-induced irreversibility generated in the trailing-edge region. The procedure starts by assuming the position of the equivalent shock, defined through its inclination with respect to section g; once the shock orientation is fixed, the mass flow rate through the nozzle passage uniquely determines the mass flux per unit area at the shock section.

Under the assumption of homentropic flow, the expansion between section g and the upstream state of the equivalent shock (uSE) is evaluated using a generalized formulation of Prandtl–Meyer expansions, as proposed by Cramer [62].

$$\mathrm{d}\delta_F = \mathrm{d}\nu = -\frac{\sqrt{M^2-1}}{M^3}\left(\frac{1}{1-\Gamma-1/M^2}\right)\mathrm{d}M \tag{8}$$

By numerically integrating Equation (8), the flow turning δ_F through the Prandtl–Meyer fan is determined, providing the flow angle β_{SE} at the upstream side of the equivalent shock. Given this angle and the previously computed unit-area mass flow G_{uSE}, the static properties can be derived from the total conditions to define the pre-shock state. The conservation of mass, energy, and momentum along the directions normal and parallel to the shock is then formulated in a generalized Rankine–Hugoniot form:

$$h_{\mathrm{dSE}} - h_{\mathrm{uSE}} = \frac{1}{2}(p_{\mathrm{dSE}} - p_{\mathrm{uSE}})\left(\frac{1}{\rho_{\mathrm{uSE}}} + \frac{1}{\rho_{\mathrm{dSE}}}\right), \tag{9}$$

$$\frac{p_{\mathrm{dSE}} - p_{\mathrm{uSE}}}{\rho_{\mathrm{uSE}} - \rho_{\mathrm{dSE}}} = (\rho_{\mathrm{uSE}}\, c_{\mathrm{uSE}}\, \sin\beta_{\mathrm{SE}})^2, \tag{10}$$

$$\rho_{\mathrm{uSE}}\, \tan\beta_{\mathrm{SE}} = \rho_{\mathrm{dSE}}\, \tan(\beta_{\mathrm{SE}} - \delta_{\mathrm{SE}}), \tag{11}$$

$$c_{\mathrm{uSE}}\, \cos\beta_{\mathrm{SE}} = c_{\mathrm{dSE}}\, \cos(\beta_{\mathrm{SE}} - \delta_{\mathrm{SE}}). \tag{12}$$

These jump relations defines the post-shock state (dSE), the flow turning across the shock δ_{SE}, and the flow angle immediately downstream of the shock. The remaining portion of the passage, from the post-shock location to exit station 2 (see Figure 3), is then resolved using the isentropic flow equations. The flow turning in this final segment is computed analogously to the nozzle deviation procedure described above, yielding a new exit flow angle. It should be noted that this angle corresponds to neither the actual exit flow nor the design target, as it represents the hypothetical angle α_2 that the flow would attain if shock-induced losses were the only irreversibilities present. Finally, the thermodynamic properties at station 2 (see Figure 3) are computed. The initially assumed shock angle is iteratively adjusted until the target exit pressure $p_2 = p_{2,\mathrm{is}} = p_{2,\mathrm{target}}$ is matched, consistent with the physical principle that stronger shocks produce larger pressure jumps whereas more oblique shocks result in smaller pressure variations. Although this equivalent shock representation simplifies the complex wave system illustrated in Figure 3, it retains the physically relevant information for preliminary design purposes; the strength of the equivalent shock is directly proportional to the degree of re-compression or re-expansion required to match the imposed downstream pressure. This means that the associated entropy generation correctly reflects the magnitude of the shock-induced irreversibility, thereby capturing the fundamental mechanism governing this loss contribution.

2.2. Compressors and Pumps

The pumps and compressors of the ORC system are modeled using a simplified black-box in–out approach based on mass and energy balances. As inputs, the model requires the mass flow rate, total-to-total pressure ratio, and inlet and outlet Mach numbers as well as the isentropic and mechanical efficiencies. Unlike turbines, losses in ORC compressors and pumps typically have much smaller impacts on the cycle performance, which justifies the adoption of a simplified model with fixed efficiencies.

2.3. Heat Exchangers

The heat exchanger model uses a generalized one-dimensional approach assuming a counter-flow configuration. The flow in both the hot and cold streams is resolved by

applying the mass conservation equation, the energy equation in terms of total enthalpy, and the momentum equation in terms of total pressure drop, which are then combined with semi-empirical correlations for the heat transfer coefficients and friction factors. Discretizing the heat exchanger along the main flow direction, the flow properties are defined at the nodal points between cells ($i = 1, 2, \ldots, n$), while heat and momentum fluxes are evaluated at the cell centers, equivalently denoted as $j = 1, 2, \ldots, n-1$ or $i + 1/2$, resulting in a finite volume scheme accurate to the second order:

$$H_{t,i+1} - H_{t,i} = \dot{Q}_{i+\frac{1}{2}}, \tag{13}$$

$$p_{t,i+1} - p_{t,i} = \Delta p_{t,i+\frac{1}{2}}, \tag{14}$$

$$\dot{Q}_j = U_j \, A_j \, \Delta T_{\mathrm{lm},j}. \tag{15}$$

Equations (13) and (14) are applied independently to the hot and cold streams. Equation (15) acts as the coupling constraint, defining the heat transfer rate as a function of the local log-mean temperature difference between the two fluids. Accordingly, this relation can be applied to either stream, depending on the side chosen as the reference for the calculation. In this regard, the heat transfer rates of the two streams generally differ, as thermal losses through the exchanger casing are accounted for through a constant shell efficiency factor $\eta = \dot{Q}_{\mathrm{cold}} / \dot{Q}_{\mathrm{hot}}$, which for simplicity is assumed to be uniform across all discretization cells.

The system is fully determined by specifying the inlet conditions for both streams, which respectively correspond to the first node of the cold stream and the last node of the hot stream. To solve the design problem, the hot side or cold side heat transfer rate is defined directly or by setting the heat exchanger efficiency in Equations (5)–(7), while Equation (15) is used for sizing purposes:

$$\varepsilon = \frac{\dot{Q}}{\dot{Q}_{\max}} \approx \frac{\dot{Q}}{\dot{C}_{\min} \, \Delta T_{|C_{\min}}} \approx \begin{cases} \dfrac{T_{\mathrm{hot,in}} - T_{\mathrm{hot,out}}}{T_{\mathrm{hot,in}} - T_{\mathrm{cold,in}}}, & \dot{C}_{\min} \text{ on hot side} \\ \dfrac{1}{\eta} \dfrac{T_{\mathrm{cold,out}} - T_{\mathrm{cold,in}}}{T_{\mathrm{hot,in}} - T_{\mathrm{cold,in}}}, & \dot{C}_{\min} \text{ on cold side} \end{cases} \tag{16}$$

where $\dot{C} = \dot{m} \, C_p$. Regarding the geometric sizing, a single-pass shell-and-tube heat exchanger is selected as the reference configuration. For simplicity and in line with the adopted one-dimensional flow formulation, this study considers a configuration without baffles.

Determining the heat transfer coefficients requires calculating local thermodynamic properties and flow velocities. The average Reynolds number (Re_h) based on hydraulic diameter is imposed on either the hot or the cold side, while the Reynolds number of the opposite stream results from the sizing procedure. For fixed mass flow rates, the prescribed Re_h controls the flow passage dimensions and convective heat transfer coefficients. The number of tubes (N_t) is specified as an additional design input. The overall heat transfer coefficient refers to the internal surface area of tube k at the cell-center location j, $U_{\mathrm{int},k,j}$, and is given by

$$U_{\mathrm{int},k,j} = \frac{1}{\dfrac{1}{h_{\mathrm{int},k,j}} + \dfrac{\ln(D_{\mathrm{ext}}/D_{\mathrm{int}})}{k_t} + \dfrac{D_{\mathrm{int}}}{D_{\mathrm{ext}}} \dfrac{1}{h_{\mathrm{ext},k,j}}} \tag{17}$$

where $h_{\mathrm{int},k,j}$ and $h_{\mathrm{ext},k,j}$ are the internal and external convective heat transfer coefficients, respectively, D_{int} and D_{ext} denote the inner and outer tube diameters, and k_t is the thermal conductivity of the tube material. Since the convective heat transfer coefficients are func-

tions of the local thermofluid dynamic states, which are defined at the nodal points, their values at the cell centers are determined through linear interpolation.

The total pressure losses on both the shell and tube sides are mainly dependent on the ratio $\Delta L_j/d_h$ between the segment (cell) length and the hydraulic diameter. At the local level, for each cell-center j, the pressure drop can be expressed as

$$\Delta p_{t,j} = \Delta p_{t,j}^{\text{fix}} + \frac{1}{2} f_j \rho_j c_j^2 \frac{\Delta L_j}{D_h}, \tag{18}$$

where f_j, ρ_j, and c_j respectively denote the friction factor, fluid density, and velocity at the cell center, ΔL_j is the length of the cell, and $\Delta p_{t,j}^{\text{fix}}$ is a user-defined pressure drop based on the detailed heat exchanger geometry assumptions; in turn, the friction factor depends on the local Reynolds number and the surface roughness. The overall length and volume of the heat exchanger can be calculated once the diameter of the tubes has been determined and the heat transfer surface has been obtained by resolving Equations (13), (15), and (17) together with the heat transfer models in Table 3. Table 3 summarizes the empirical models for convective heat transfer coefficients and friction factors for both single-phase and two-phase flows, all of which have been validated in the existing literature. Specifying the tube material, thickness, and surface roughness completes the definition of the problem. Additionally, the tube thermal conductivity is assumed to be constant with temperature and dependent only on the tube material.

Table 3. Empirical models used for convective heat transfer coefficients and friction factor in the heat exchanger.

Quantity	Case	Model	Reference
h [W m^{-2} K^{-1}]	Single-phase turbulent	Dittus–Boelter	[63]
h [W m^{-2} K^{-1}]	Single-phase laminar	Sieder–Tate	[63]
h [W m^{-2} K^{-1}]	Evaporation	Mahmoud et al.	[64]
h [W m^{-2} K^{-1}]	Condensation	Shah	[65]
f [−]	Single-phase	Haaland	[66]
f [−]	Two-phase	Ribatski et al.	[67]

2.4. WHR System

The system-level model couples the components to ensure continuity of the fluid dynamic and thermodynamic variables. The connecting pipes are not modeled explicitly, but are assumed to be isentropic and adiabatic so that total quantities are conserved; in contrast, static properties may vary due to changes in cross-sectional area between the outlet of one component and the inlet of the next. Further details on the system components are provided in the Results section, which presents the layouts selected for the case studies.

2.5. Validation

The experimental results reported by Sung et al. [68] provide a detailed validation dataset for the ORC model described above. Both the experimental and simulated cycles are represented in the T–s thermodynamic diagram shown in Figure 4. The reference layout corresponds to a simple ORC system using R245fa, as working fluid designed for a nominal net power output of 250 kW and consisting of a feed pump, evaporator, radial inflow turbine, and condenser together with auxiliary units employed to emulate the heat source and cold sink.

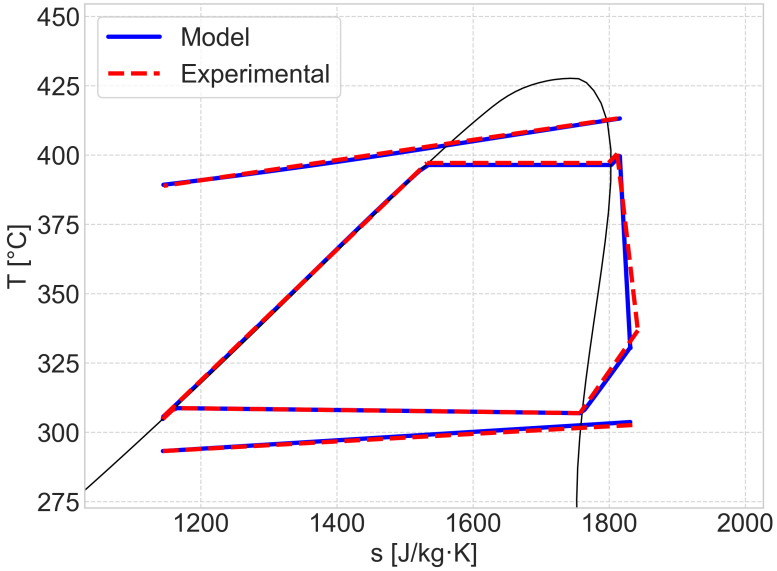


Figure 4. Comparison between model predictions and experimental data in the T–s plane. The black line represents the saturation curve.

For the validation procedure, the model inputs are adjusted to match the control variables reported in the experimental campaign. In particular, the condenser outlet temperature (T_1), pump inlet temperature ($T_{1'}$), pump discharge pressure (p_2), and exhaust gas temperature at the outlet of the main heat exchanger (T_{stack}) are imposed, together with the boundary conditions of the heat source and cold sink. The resulting performance indicators, corresponding to the cycles shown in Figure 4, are summarized numerically in Table 4.

Table 4. Comparison between model predictions and experimental data.

Output Variable	Model Value	Experimental Value	Residual [%]
T_2 [K]	305.59	305.67	−0.03
T_3 [K]	399.54	400.41	−0.22
T_4 [K]	330.54	336.65	−1.81
p_4 [bar]	2.01	2.20	−8.63
P_{net} [kW]	251.02	248.10	+1.18

Overall, the model exhibits a high level of accuracy, with thermodynamic properties at most cycle state points deviating from the experimental measurements by less than 0.25%. The largest discrepancies are observed at the turbine outlet, where the model underestimates the temperature by approximately 1.8% and the pressure by about 8%. As an additional assessment of the turbine model, a model-to-model comparison with the preliminary design framework of Da Lio et al. [40] was carried out to evaluate the total-to-static efficiency as a function of the volumetric flow ratio VR and size parameter SP at optimal design operating conditions ($\phi = \phi_{\text{opt}}$, $\psi = \psi_{\text{opt}}$). This comparison is of particular interest because VR and SP are both parameters that are widely employed in the literature to construct turbine design maps. The results show good overall agreement between the two models, with a maximum deviation slightly above 3% over the investigated ranges, confirming that the present model correctly captures the main trends of turbine performance with respect to these two variables. This comparison is not reported here for the sake of brevity.

3. Case Study for WHR Application

The modeling framework presented in the preceding sections is applied here to a WHR system integrated with a turbocharged ICE fueled by bio-ethanol. The engine's characteristics and boundary conditions are described in Section 3.1. The primary objective of this analysis is to assess the ability of the proposed model to qualitatively capture the key design tradeoffs inherent to WHR systems of this class. These include the thermal coupling between the recovery system and the ICE exhaust stream, the sizing and performance of the main heat exchanger and condenser, the aerodynamic and loss mechanisms governing the radial inflow turbine design, and the influence of the working fluid selection and operating variables on overall system performance. The above aspects are addressed in Sections 3.2–3.6.

3.1. Case Study and Setup

The engine at the heart of the system is a prototype derived from a commercial Compressed Natural Gas (CNG) spark-ignition engine, itself adapted from a Compression Ignition (CI) platform of the same displacement [69] and subsequently modified to run on pure bioethanol by replacing the methane injection system [70]. Its full thermodynamic characterization and one-dimensional model, which supply the boundary conditions for the present analysis, are reported in [27]. The reference operating point corresponds to the minimum-BSFC condition of the standalone ICE, representing optimal engine operation prior to WHR integration. However, the coupling between the two systems is not entirely neglected; the back-pressure imposed by the WHR system on the engine exhaust is accounted for by following the approach described in Section 3.2.

The system layout comprises a pump-compressor, a main heat exchanger, a radial inflow turbine (RIT_1), and an air-cooled condenser served by an electrically driven fan. A two-stage configuration featuring an additional turbine stage (RIT_2) is also considered, as illustrated in Figure 5.

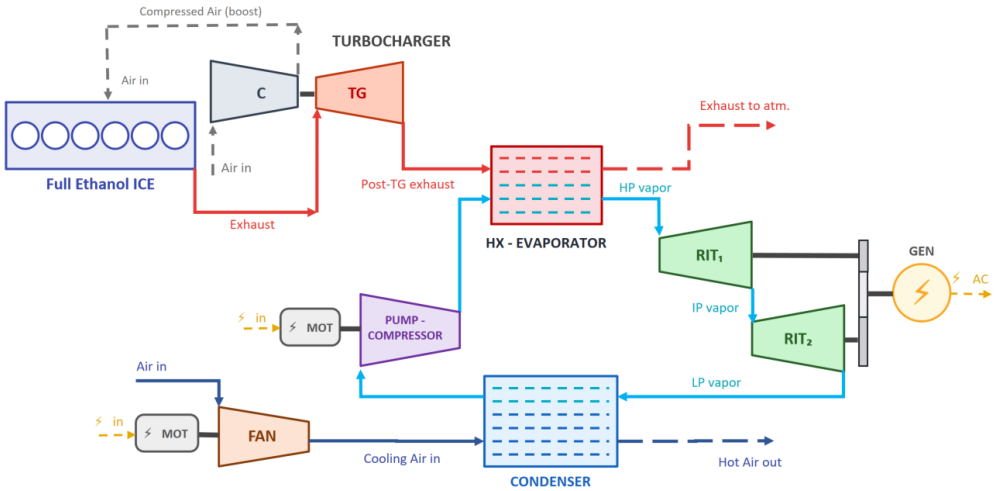


Figure 5. Schematic of the WHR system integrated with the turbocharged ICE.

Five working fluids are considered, spanning a broad range of thermophysical properties and fluid families and selected based on environmental criteria such as GWP, flammability, and thermodynamic suitability for the operating range of interest. Their main characteristics are reported in Table 5. The saturation pressure is included at a temperature slightly above ambient, taken as 300 K as a reference, since it represents the expected condensation pressure and will prove to be a key factor in the subsequent analysis.

A hard upper bound on the cycle maximum temperature is imposed by the thermal stability limit T_{lim}, beyond which irreversible fluid decomposition occurs. Since the Ozone Depletion Potential (ODP) is zero for all fluids considered here, it is not included in the table.

Table 5. Main thermophysical and environmental properties of the working fluids considered in the study.

Fluid	T_{nb} [K]	p_{cr} [bar]	$p_{cond,300K}$ [bar]	T_{lim} [K]	M_w [g/mol]	GWP [-]	Flamm.
Ethanol	351.4	61.4	0.29	650 [b]	46.1	1 [c]	Yes [d]
Isobutane	261.4	36.3	3.10	593 [a]	58.1	3 [a]	Yes [a]
MM	374.7	19.2	0.37	573 [a]	162.4	0 [a]	Yes [a]
R1234ze(E)	254.2	36.4	4.10	500 [e]	114.0	4 [f]	Moderate [f]
Toluene	383.8	41.1	0.08	673 [a]	92.1	3.3 [a]	Yes [a]

[a] [71]. [b] Upper temperature limit as implemented in CoolProp [37]. [c] Ethanol is not classified as a greenhouse gas by the IPCC [72]. [d] [73]. [e] [74]. [f] [75].

A preliminary assessment of the system is performed by keeping a subset of variables fixed, as reported in the lower portion of Table 6, while a limited number of design variables and the working fluid are varied (see Table 7). The boundary conditions of the source and sink streams are also summarized in Table 6. The selected turbine design parameters fall within the typical ranges reported in the turbomachinery literature for radial inflow turbines, ensuring consistency with established design practices [39,76]. Other geometrical parameters, including tip clearance, stator-to-rotor radial gap, backplate clearance, and trailing edge thickness, are selected within conventional ranges consistent with studies reported in the literature [77–80]. Regarding the heat exchangers, Aluminum 6061-T6 is assumed for the condenser and Inconel 617 for the evaporator, as their thermal conductivity and yield strength are used as input parameters in the heat exchanger model to account for both heat transfer and structural constraints.

Table 6. Summary of the boundary conditions and fixed input parameters for the WHR case study.

Component	Parameter	Symbol	Value
Source Boundary Conditions			
Source/Exhaust Gas	Fluid composition (mass-based)	—	69.4% N_2, 12.2% CO_2, 18.4% H_2O
	Mass flow rate	$\dot{m}_{exh}$	0.220 kg/s
	Inlet temperature	T_{exh}	993.10 K
	Exhaust pipe diameter	D_{pipe}	0.064 m
	Exhaust discharge total pressure	$p_{t,dis,exh}$	1 atm
Sink Boundary Conditions			
Sink/Ambient Air	Fluid composition (mass-based)	—	75.5% N_2, 23.1% O_2, 1.4% Ar
	Ambient temperature	T_{amb}	288.0 K
	Ambient pressure	P_{amb}	1 atm
	Air discharge total pressure	$P_{dis,air}$	1 atm
Parameters			
ORC/Brayton Cycle	Subcooling (Pump Inlet)	ΔT_{sc}	0.0 K (saturated inlet)
Pump/Compressor	Inlet Mach number	$M_{in,comp}$	0.003
	Isentropic efficiency (tt)	$\eta_{tt,comp}$	0.85
	Mechanical efficiency	$\eta_{m,comp}$	0.98

Table 6. *Cont.*

Component	Parameter	Symbol	Value
Radial Turbine	Inlet Mach number	$M_{\text{in,turb}}$	0.10
	Work coefficient	ψ_{is}	1.40
	Flow coefficient	ϕ_{is}	0.35
	Channel width ratio	b_3^*	0.04
	Meridional velocity ratio	MVR_{is}	1.10
	Rotor diameter ratio	X_r	1.10
	Volute diameter ratio	X_v	1.20
	Volute aspect ratio	AR_v	1.50
	Rotor outlet flow angle	$\alpha_{4,\text{is}}$	90°
	Rotor axial length ratio	$l_{z,r}^*$	0.30
	Nozzle–rotor radial gap	ϵ_i^*	0.02
	Rotor tip clearance	ϵ_r^*	0.02
	Rotor–backplate axial gap	ϵ_b^*	0.02
	Nozzle trailing-edge thickness	$t_{\text{te,n}}^*$	0.05
	Mechanical efficiency	$\eta_{\text{m,turb}}$	0.98
Main HX/Evaporator	Efficiency	ε_{HX}	0.90
	Shell efficiency	η_{HX}	0.99
	Exhaust-side Reynolds number	$Re_{\text{exh,HX}}$	0.50×10^4
	Number of tubes	$N_{t,\text{HX}}$	50
	Material	—	Inconel 617 ($k = 25\,\text{W}/(\text{m}\cdot\text{K})$, $\sigma_y = 240\,\text{MPa}$)
Condenser	Air-side Reynolds number	$Re_{\text{air,CO}}$	2.90×10^4
	Shell efficiency	η_{CO}	0.99
	Fan isentropic efficiency (tt)	$\eta_{\text{tt,fan}}$	0.85
	Fan electrical efficiency	$\eta_{\text{el,fan}}$	0.98
	Material	—	Al-6061-T6 ($k = 167\,\text{W}/(\text{m}\cdot\text{K})$, $\sigma_y = 240\,\text{MPa}$)

Table 7. Reference values of the design variables for each working fluid.

Description	Symbol	Ethanol	Isobutane	MM	R1234ze(E)	Toluene
Air-to-cycle mass flow ratio (condenser)	$\dot{m}_{\text{air,cond}}/\dot{m}_{\text{cycle}}$	36	17	10	15	19
Cycle-to-exhaust mass flow ratio	$\dot{m}_{\text{cycle}}/\dot{m}_{\text{exh}}$	0.46	1.0	1.15	1.7	0.88
Minimum cycle temperature	$T_{\text{min,cycle}}$ [K]	327.5	315	315	315	330
Maximum cycle total pressure	$p_{\text{t,max,cycle}}$ [bar]	8.5–50	20	8	110	4–30
Number of tubes (Condenser)	$N_{t,\text{CO}}$	350	350	350	350	350

The reference ORC cycle using ethanol as working fluid is shown in the T–s plane in Figure 6, together with the temperature profiles of the exhaust gas and cooling air. A distinctive feature of the model is the inclusion of connecting ducts between components, which are treated as isentropic flows with varying cross-sectional area. As illustrated in the insets, these ducts modify the static thermodynamic states between components while preserving total quantities, resulting in a mismatch between component outlet and inlet states. In the T–s plane, this appears as vertical transformations. The duct between the turbine outlet and the condenser inlet acts as a diffuser due to the larger downstream cross-section, causing a slight isentropic recompression and implicitly accounting for the turbine diffuser. Conversely, the duct between the condenser outlet and pump inlet behaves as a convergent passage, leading to a lower static temperature at the pump inlet despite saturated liquid conditions.

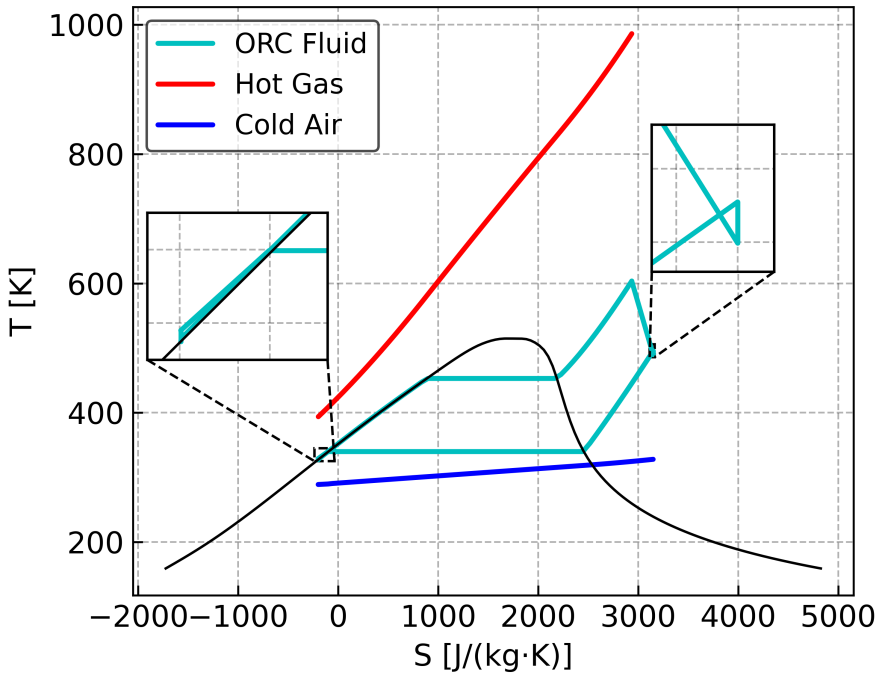


Figure 6. Reference ORC cycle for ethanol in the T–s plane. The black line represents the saturation curve.

The magnitude of this effect is governed by the inlet Mach number $M_{in,\mathrm{comp}}$, which controls the pump inlet cross-section. As shown in Figure 7, increasing $M_{in,\mathrm{comp}}$ reduces the pump inlet section, resulting in a larger difference between the static pressure at the condenser outlet and at the pump inlet and consequently in a larger mismatch between the condensation temperature and the minimum cycle temperature $T_{\mathrm{min,cycle}}$ (located at the pump inlet).

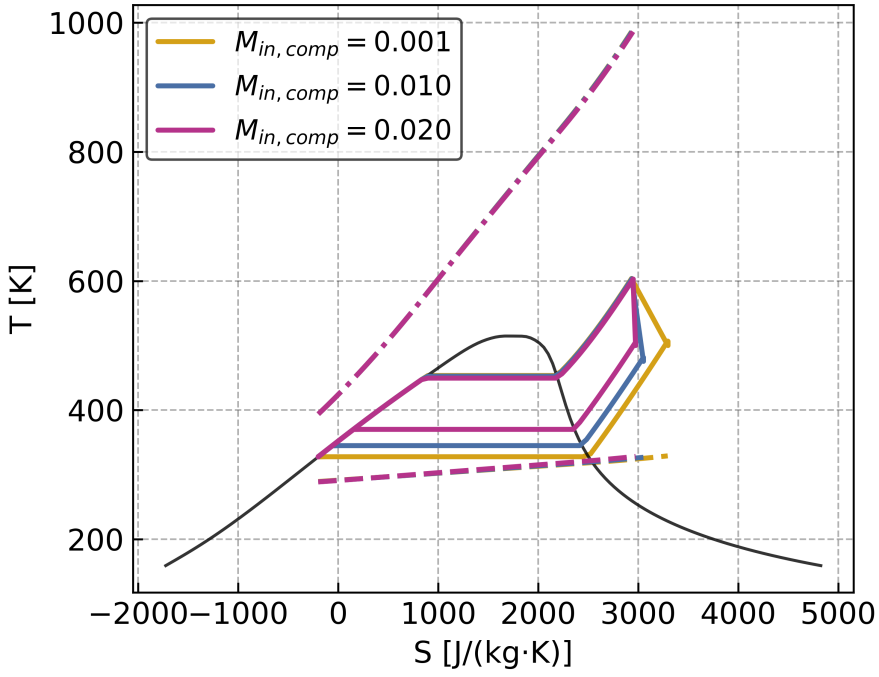


Figure 7. Effect of the pump inlet Mach number $M_{in,\mathrm{comp}}$ on the ORC cycle shape in the T–s plane for ethanol. The black line represents the saturation curve.

This also affects the expansion ratio of the cycle, with a direct impact on turbine efficiency. These effects have a significant impact on system performance. In particular, although the condensation temperature is indirectly controlled through $T_{\mathrm{min,cycle}}$, it still has a strong influence on both cycle efficiency and condenser design, as discussed in the following sections. Similarly, the expansion ratio plays a key role in determining turbine efficiency. The reference value of $M_{in,\mathrm{comp}}$ reported in Table 7 represents a compromise between these competing effects.

3.2. Main HX and ICE Coupling

The preliminary analysis of the main heat exchanger is presented in Figure 8. The key quantity governing selection of the design parameters is the total pressure drop of the exhaust gases across the heat exchanger $\Delta P_{t,HX}$, shown as contour lines in the right panel. Since the exhaust discharge pressure is fixed at ambient conditions, any pressure drop across the heat exchanger directly translates into an increased back-pressure at the ICE turbocharger turbine outlet.

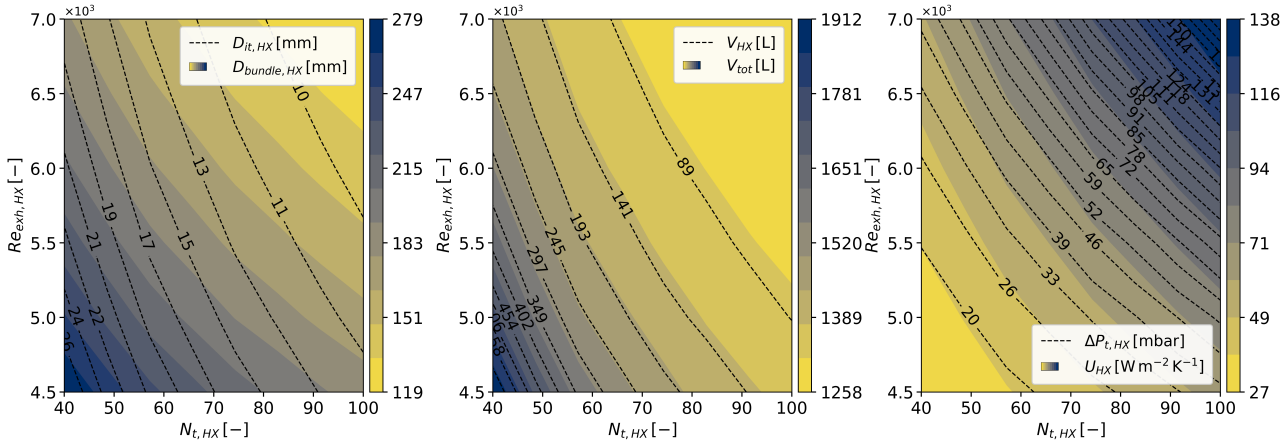


Figure 8. Preliminary main heat exchanger analysis for ethanol as the working fluid. Contour maps of the internal tube diameter $D_{it,\mathrm{HX}}$ and bundle diameter $D_{bundle,\mathrm{HX}}$ (**left**), heat exchanger volume V_{HX}, and total volume V_{tot} (**center**) and of the overall heat transfer coefficient U_{HX} and total pressure drop $\Delta P_{t,\mathrm{HX}}$ (**right**) as functions of the number of tubes $N_{t,\mathrm{HX}}$ and the exhaust-side Reynolds number $Re_{\mathrm{exh,HX}}$.

The present WHR system model and the ICE model of Giglio et al. [27] are decoupled, as they are run independently; however, to partially account for the ICE-WHR coupling, an iterative calibration was performed on the reference operating point (Figure 6). The $\Delta P_{t,HX}$ computed by the WHR model was imposed as an additional back-pressure boundary condition in the ICE model, which was then re-run to provide an updated exhaust mass flow rate and temperature, and consequently a new $\Delta P_{t,HX}$ from the WHR model. A threshold of approximately 20 mbar was identified as the maximum acceptable back-pressure. Beyond this value, the engine operating point undergoes a significant shift compared to the reference case with discharge at ambient pressure, potentially leading to the onset of knock and a reduction in the surge margin of the turbocharger compressor. As a consequence, the exhaust gas conditions can no longer be considered reliable. Therefore, the exhaust boundary conditions reported in Table 6 are the result of this single-point calibration and are kept fixed throughout the entire parametric study. It follows that results obtained for cycle configurations corresponding to $\Delta P_{t,HX}$ values significantly deviating from this 20 mbar target should be interpreted with caution, as they would imply exhaust conditions different from those assumed, potentially affecting the reliability of the predicted system performance.

As shown in Figure 8, both $N_{t,HX}$ and $Re_{exh,HX}$ govern a tradeoff between heat exchanger compactness and pressure drop. Increasing $N_{t,HX}$ reduces the tube diameter and the overall volume, but at the cost of higher $\Delta P_{t,HX}$. Similarly, higher $Re_{exh,HX}$ improves the heat transfer coefficient and reduces the required heat transfer surface, but also leads to larger pressure losses. Although the 20 mbar constraint forces a larger heat exchanger, its impact on the total system volume remains limited because the condenser is on average significantly larger than the main heat exchanger and consequently dominates the total volume budget, as shown in the central panel of Figure 8. The selected values of $N_{t,HX}$ and $Re_{exh,HX}$ reported in Table 6 correspond to the 20 mbar back-pressure target.

3.3. Condenser and Sink Flow Analysis

The purpose of this analysis is to determine the operability range with respect to the condenser and sink flow design variables for each working fluid. Figures 9 and 10 illustrate these analyses for ethanol as a representative working fluid.

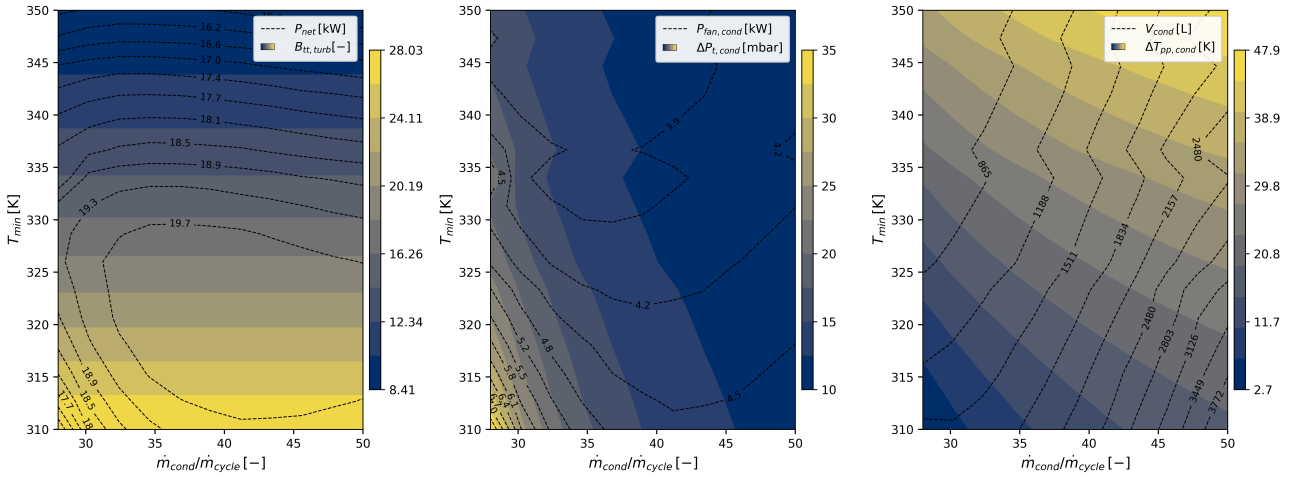


Figure 9. Preliminary condenser analysis for ethanol as the working fluid. Contour maps of the net power output P_{net} and turbine pressure ratio $B_{tt,\text{turb}}$ (**left**), fan power $P_{\text{fan,cond}}$, and condenser total pressure drop $\Delta P_{t,\text{cond}}$ (**center**) and of the condenser volume V_{cond} and pinch point temperature difference $\Delta T_{pp,\text{cond}}$ (**right**) as functions of the air-to-cycle mass flow ratio $\dot{m}_{\text{air,cond}}/\dot{m}_{\text{cycle}}$ and the minimum cycle temperature $T_{\text{min,cycle}}$.

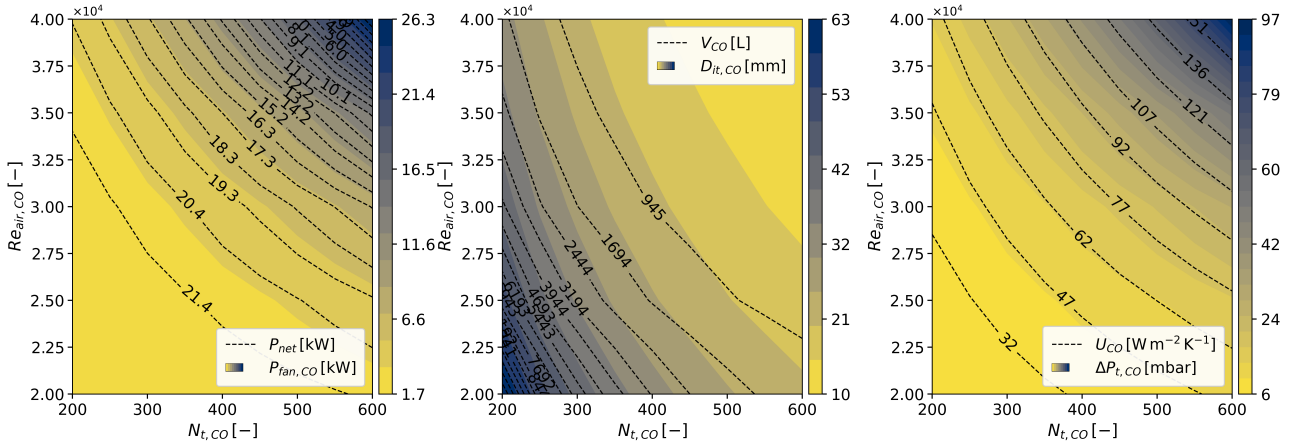


Figure 10. Preliminary condenser analysis for ethanol as working fluid. Contour maps of the net power output P_{net} and fan power $P_{\text{fan,cond}}$ (**left**), condenser volume V_{cond}, and internal tube diameter $D_{it,\text{cond}}$ (**center**) and of the overall heat transfer coefficient U_{cond} and total pressure drop $\Delta P_{t,\text{cond}}$ (**right**) as functions of the number of condenser tubes $N_{t,\text{CO}}$ and the sink-side Reynolds number $Re_{\text{air,CO}}$.

The first analysis is carried out by varying $\dot{m}_{\text{air,cond}}/\dot{m}_{\text{cycle}}$ and $T_{\text{min,cycle}}$ while keeping all other variables fixed at the reference values reported in Table 7. For both variables, the results clearly show the presence of optimal operating conditions arising from competing physical mechanisms.

For $\dot{m}_{\text{air,cond}}/\dot{m}_{\text{cycle}}$, the optimum results from the tradeoff between heat transfer performance and auxiliary consumption. Increasing the air mass flow rate reduces the temperature rise of the cooling stream, lowering the log-mean temperature difference and requiring a larger heat transfer surface. At the same time, the fan power exhibits a non-monotonic behavior: while higher flow rates reduce frictional losses per unit length, the increase in mass flow eventually dominates, leading to higher auxiliary consumption.

A similar tradeoff governs the effect of $T_{\text{min,cycle}}$: lower values reduce the pinch point temperature difference and increase the required heat transfer surface, but also lead to higher expansion ratios and improved cycle performance. As a consequence, the net power output P_{net} is maximized at intermediate values of $\dot{m}_{\text{air,cond}}/\dot{m}_{\text{cycle}}$ and low $T_{\text{min,cycle}}$, where the combined effect of turbine performance and auxiliary consumption is most favorable.

The influence of the number of condenser tubes $N_{t,\text{CO}}$ and the sink-side Reynolds number $Re_{\text{air,CO}}$ on condenser performance and sizing is analyzed in Figure 10. In contrast to the previous analysis, no well-defined optimum is observed, as the governing mechanisms lead to largely monotonic trends. For the main heat exchanger, the selection of $N_{t,\text{CO}}$ and $Re_{\text{air,CO}}$ reflects a design compromise between heat transfer performance, condenser compactness, and auxiliary power consumption.

3.4. Effects of Mass Flow and Pressure Ratio

The feasible operating range in terms of the cycle-to-exhaust mass flow ratio $\frac{\dot{m}_{\text{cycle}}}{\dot{m}_{\text{exh}}}$ and corresponding net power output achieved with a single RIT stage P_{net} is shown in Figure 11 for all five working fluids. For each fluid, results are presented as a band: the upper boundary corresponds to the optimal total-to-total pressure ratio $B_{tt,\text{turb}}$, while the lower boundary corresponds to the minimum pressure ratio considered. As detailed in Section 3.5, the net power output exhibits a maximum at a specific pressure ratio. This behavior arises because turbine efficiency generally decreases with increasing pressure ratio, as evident in the same figure. Consequently, the gain associated with a higher expansion ratio is progressively offset by the efficiency drop, leading to an optimal operating point.

The presence of an optimal $\dot{m}_{\text{cycle}}/\dot{m}_{\text{exh}}$ reflects two competing effects. Because the heat exchanger efficiency ε_{HX} is constant, the thermal power transferred to the working fluid in the evaporator is also constant; therefore, as the mass flow rate decreases, the specific enthalpy rise increases, leading to a higher maximum cycle temperature $T_{\text{max,cycle}}$ and improved thermodynamic efficiency. Conversely, increasing the mass flow rate reduces the specific enthalpy rise and consequently $T_{\text{max,cycle}}$, approaching the dew point at the evaporator outlet. In the low mass flow rate region, the increase in thermodynamic efficiency dominates over the reduction in mass flow rate, leading to an increase in P_{net}. In contrast, the decrease in efficiency becomes dominant at higher mass flow rates, with P_{net} decreasing despite the larger flow rate. The upper bound of the feasible range is set by the requirement of superheated vapor at the evaporator outlet, which is necessary for safe turbine operation, while the lower bound is imposed by the thermal stability limit T_{lim} (Table 5), which is exceeded at very low mass flow rates. Ethanol and toluene exhibit the highest net power output with a single turbine stage, while the remaining fluids show lower performance. The feasible ranges vary significantly among fluids in bot h$\dot{m}_{\text{cycle}}/\dot{m}_{\text{exhaust}}$ and band width, reflecting differences in thermophysical properties (Table 5).

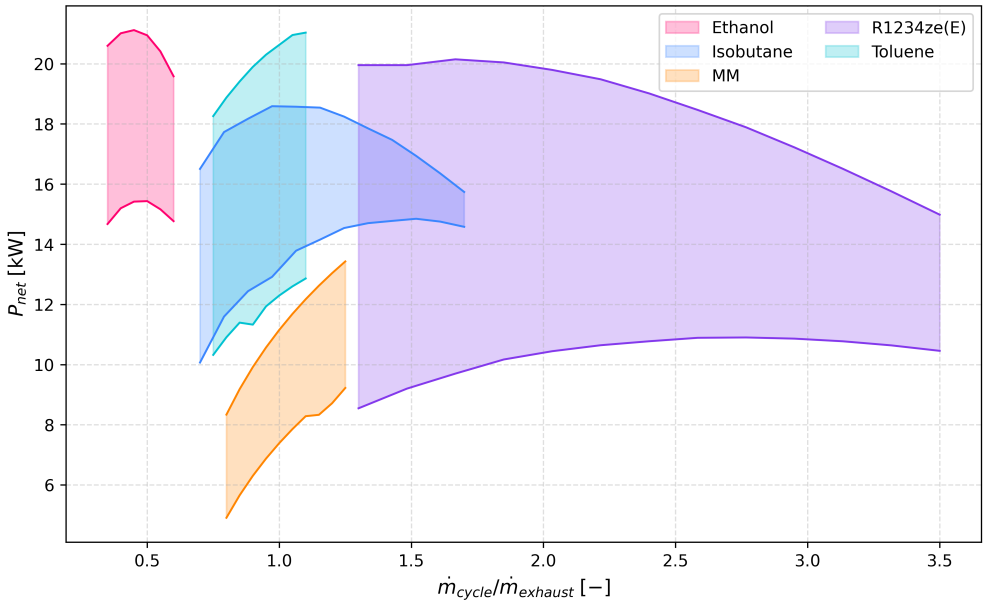


Figure 11. Net power output P_{net} as a function of cycle-to-exhaust mass flow ratio $\dot{m}_{\text{cycle}}/\dot{m}_{\text{exh}}$ for five working fluids. For each band, the span is from the minimum total-to-total pressure ratio explored to the optimal single-stage value. Results refer to the single-stage turbine configuration.

Figure 12 reports the turbine total-to-total efficiency η_{tt} and the corresponding loss breakdown at these optimal operating points. All cases operate under trans-sonic conditions with supersonic flow in the nozzle, meaning that shock losses are present for all fluids. Rotor passage loss is the dominant contribution in all cases, followed by rotor tip clearance and nozzle profile losses. The nozzle shock loss introduced in the present model represents a non-negligible contribution, highlighting its relevance in the preliminary design of ORC turbines operating at high expansion ratios. Rotor disk and volute friction losses are comparatively small.

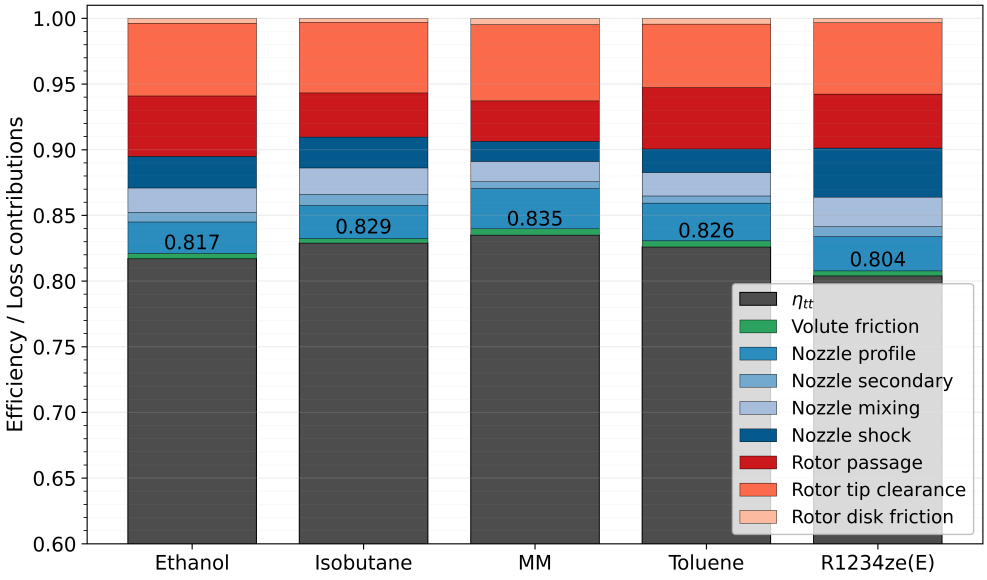


Figure 12. Turbine total-to-total efficiency η_{tt} and loss breakdown at the peak net power operating point for each working fluid, corresponding to the optimal single-stage total-to-total pressure ratio.

The relative contribution of each loss mechanism varies across the cases with different working fluids, reflecting differences in inlet flow conditions, pressure ratio, and fluid properties, which in turn influence turbine geometry and key operating parameters such as

rotational speed and flow velocities at the various sections. In particular, the shock-induced loss contribution is found to range approximately from 0.02 to 0.04 total-to-total efficiency points across the optimal operating conditions investigated here, highlighting the non-negligible impact of a term that is either neglected or oversimplified in most preliminary design models available in the literature.

It should be noted that in the present design model the turbine tip clearance is defined as a percentage of the rotor diameter, which is itself an output of the design process. As a result, the tip clearance scales linearly with the rotor size. However, this linear scaling is no longer realistic, since the resulting clearance would be too small to be technologically feasible. This is especially the case for small-scale machines, as shown later for supercritical cases with high inlet fluid density. Therefore, these results should be interpreted qualitatively, taking into account the limitations of the adopted design approach. This aspect is particularly important given that tip clearance losses represent a significant contribution to the overall loss budget, as clearly shown in Figure 12.

3.5. Multistage RIT Configuration

The transition from a single-stage to a two-stage turbine configuration is illustrated in Figure 13 for ethanol. This is representative of the behavior observed across all fluids, with variations depending on the thermodynamic region of operation.

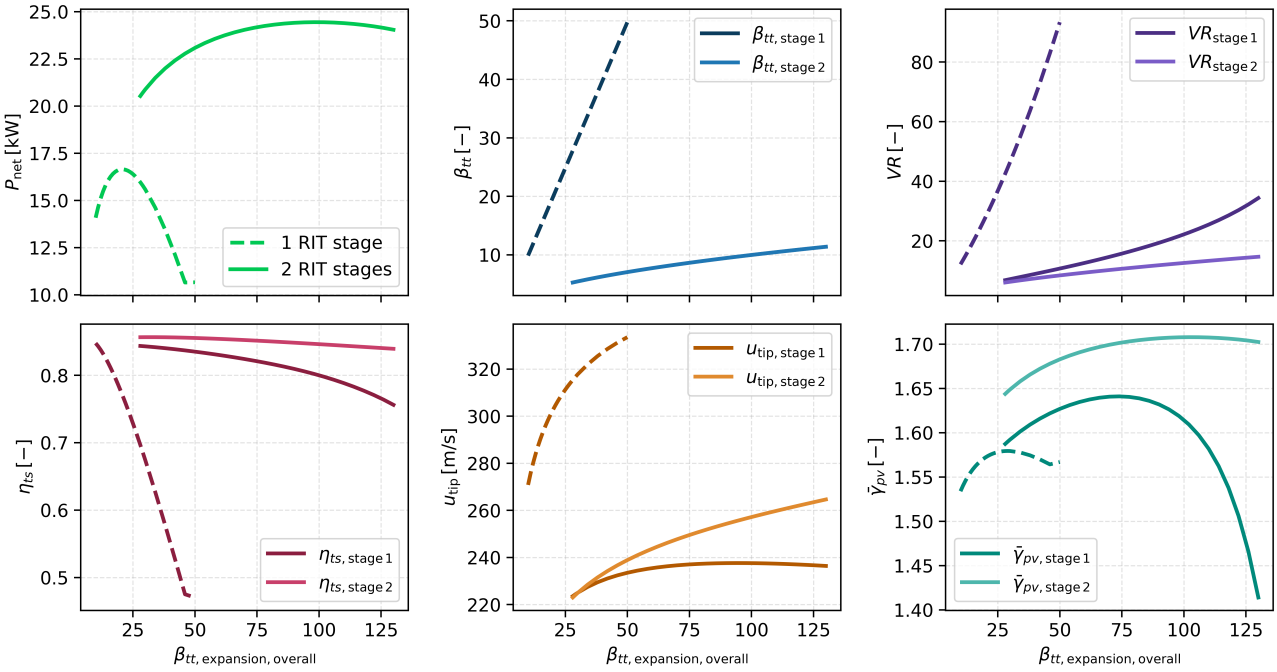


Figure 13. Comparison between single-stage (dashed) and two-stage (solid) radial inflow turbine configurations for ethanol as the working fluid as a function of the overall total-to-total expansion ratio $\beta_{tt,\text{expansion,overall}}$. (**Top row**): Net power output P_{net}, stage pressure ratios $\beta_{tt,\text{stage}\,1}$ and $\beta_{tt,\text{stage}\,2}$, and stage volume ratios $VR_{\text{stage}\,1}$ and $VR_{\text{stage}\,2}$. (**Bottom row**): Total-to-static efficiency η_{ts}, rotor tip speed u_{tip}, and mean isentropic exponent $\bar{\gamma}_{pv}$ for each stage.

The dashed curves correspond to the single-stage layout. The net power output P_{net} exhibits a clear maximum as a function of the overall expansion ratio $\beta_{tt,\text{expansion,overall}}$, consistent with the upper boundary in Figure 11. This optimum arises from the decrease in stage efficiency with increasing β_{tt}; beyond a certain point, the drop in total-to-static efficiency η_{ts} outweighs the benefit of larger expansion, leading to a decline in P_{net}. In addition, the rotor tip speed u_{tip} increases rapidly with β_{tt} and approaches the structural limit. When either u_{tip} exceeds this limit (550 m/s in this study) or when η_{ts} falls below

an acceptable value, the single-stage solution is no longer viable. In the present modeling framework, the occurrence of either of these conditions automatically triggers a transition to a two-stage radial inflow turbine configuration.

In the two-stage configuration, the overall expansion is equally split in terms of pressure ratio. However, due to real gas effects, equal pressure ratios do not correspond to equal volume ratios VR, since the mean isentropic exponent $\bar{\gamma}_{pv}$ (evaluated as an average between the inlet and outlet of each stage in Figure 14) varies with the local thermodynamic state. This effect becomes particularly relevant for cycles operating at high maximum pressures, where the inlet of the first stage lies in non-ideal thermodynamic regions (e.g., dense vapor or supercritical conditions). As a result, even with identical pressure ratios, the two stages experience significantly different volume ratios and inlet conditions, leading to stage imbalance not only in terms of thermodynamic state but also in performance. In particular, the total-to-static efficiency η_{ts} differs between stages, in agreement with literature correlations that relate turbine efficiency to the volume ratio VR. This implies that an equal pressure ratio split does not correspond to an optimal distribution of the expansion. A more appropriate design would require a non-uniform pressure ratio allocation to achieve a more balanced VR and efficiency between stages. However, such an optimization lies beyond the scope of the present work. Nonetheless, these results highlight the importance of accounting for real gas effects in the design of multistage ORC turbines, especially under high-pressure operating conditions.

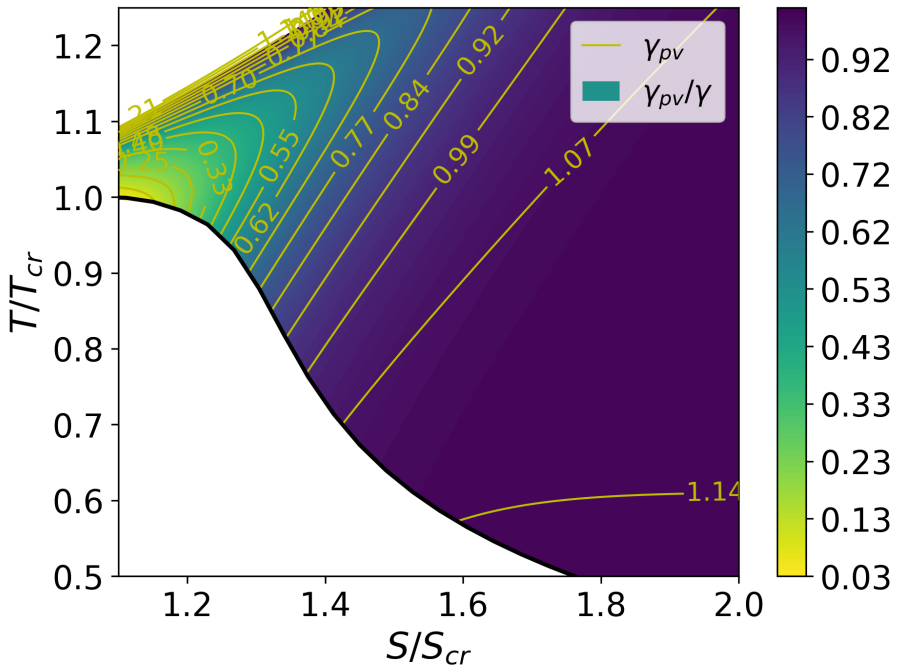


Figure 14. Isentropic pressure–volume exponent γ_{pv} (contour lines) and ratio γ_{pv}/γ (color map) for ethanol in the reduced temperature–entropy plane T/T_{cr}–S/S_{cr}. The saturation curve is shown as a solid black line.

3.6. Parametric Analysis

The full parametric study is summarized in Table 8, which reports the discrete levels explored for each design variable and working fluid. For each parameter, the investigated range is centered around the reference values introduced in Table 7. By simultaneously varying $T_{\text{min,cycle}}$ (thus, the condensation pressure) and $P_{\text{t,max,cycle}}$, different overall expansion ratios of the cycle are explored.

Table 8. Discrete levels of the design variables explored in the parametric study for each working fluid.

Parameter	Ethanol	R1234ze(E)	Toluene	Total Cases [-]
$\dot{m}_{air,cond}/\dot{m}_{cycle}$ [-]	30, 37, 44	10, 15, 20	14, 19, 24	-
$\dot{m}_{cycle}/\dot{m}_{exh}$ [-]	0.42, 0.44, 0.46 0.48, 0.50	1.3, 1.5, 1.7 1.9, 2.1	0.8, 0.84, 0.88 0.92, 0.96	-
$T_{min,cycle}$ [K]	315, 327.5, 340	310, 315, 320	320, 330, 340	-
$P_{t,max,cycle}$ [bar]	8.7, 50.0	110	4, 25	-
$N_{t,CO}$ [-]	300, 400, 500	300, 400, 500	300, 400, 500	-
Total cases [-]	270	135	270	675

For working fluids such as R1234ze(E), which condenses at relatively high pressures (Table 5) even at near-ambient temperatures, the resulting overall expansion ratios remain limited and do not reach values requiring a two-stage turbine configuration. For this reason, only a single value of $P_{t,max,cycle}$ is considered for this fluid, corresponding to the optimal value identified in the preliminary analyses while respecting structural pressure limits (set to 120 bar). In practice, the maximum pressure explored may be lower than these limits (see Table 8), since at high $P_{t,max,cycle}$ the turbine inlet density increases significantly due to operation in dense vapor or supercritical conditions. This results in very compact turbine geometries and consequently in excessively high rotational speeds, which act as an additional limiting factor on the admissible maximum pressure. For ethanol and toluene, the lower condensation pressures (Table 5) enable significantly higher expansion ratios compatible with multistage turbine configurations. Therefore, multiple values of $P_{t,max,cycle}$ are explored for these fluids to capture both single- and two-stage RIT operation, as observed in Figures 11 and 13, where two distinct operating regions can be clearly identified. The first, at high pressure ratios, corresponds to a two-stage RIT configuration, while the second occurs at lower pressure ratios where a single-stage RIT is sufficient. The design space is further constrained by a set of physical and technological limits. First, the maximum cycle temperature is bounded by the thermal stability limit of each working fluid (Table 5). In addition, a maximum rotational speed of 500,000 rpm is imposed for the turbine, together with a minimum turbine rotor diameter of 2.5 cm to ensure mechanical feasibility. Finally, all configurations leading to two-phase flow conditions within the turbine are excluded from the analysis. Only the configurations satisfying these constraints are reported in the following figures.

Figure 15 highlights the tradeoff between net power output and system size. In general, increasing the turbine volume leads to higher P_{net}, although the benefit progressively saturates, indicating diminishing gains beyond a certain size. The feasible designs span approximately from 10 to 22 kW for single-stage RIT configurations and from 24 to 36 kW for two-stage configurations, with total volumes ranging from about 600 to 9000 L. Among the working fluids considered here, ethanol provides the best overall performance for the present case study.

Figure 16 provides further insight into the distribution of feasible designs in the V–P_{net} space, with the color maps showing that these regions correspond to markedly different operating conditions. In particular, two-stage configurations are generally associated with higher T_{max} and with distinct rotational speed levels for each stage, typically on the order of 100,000–300,000 rpm for the first stage and 40,000–100,000 rpm for the second stage. This reflects the fact that the two turbine stages operate under significantly different thermodynamic and inlet flow conditions. The pressure drop in the main heat exchanger shows only limited deviation from the target value defined in the previous section, indicating that the results can be considered reliable.

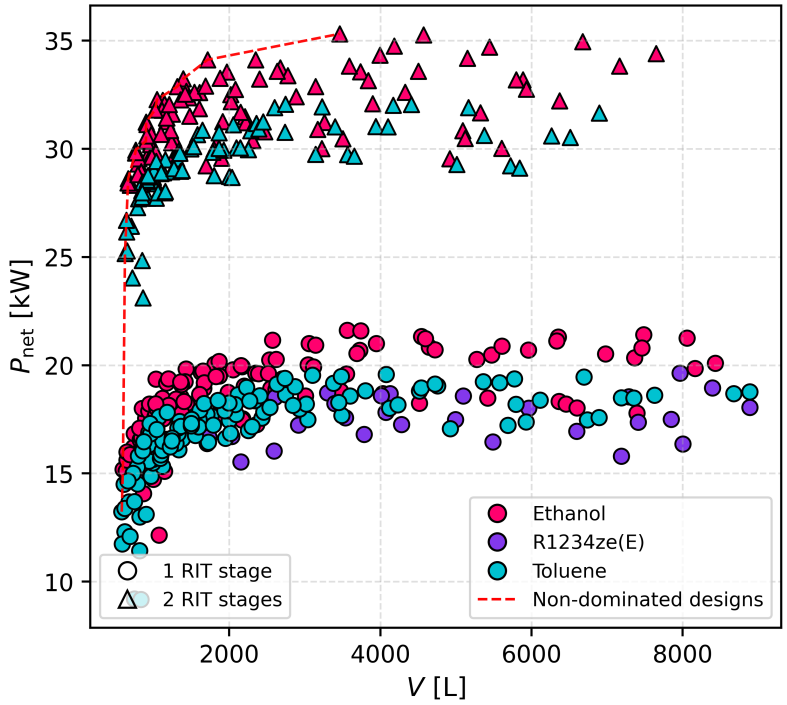


Figure 15. Net power output as a function of turbine volume for different working fluids and turbine configurations.

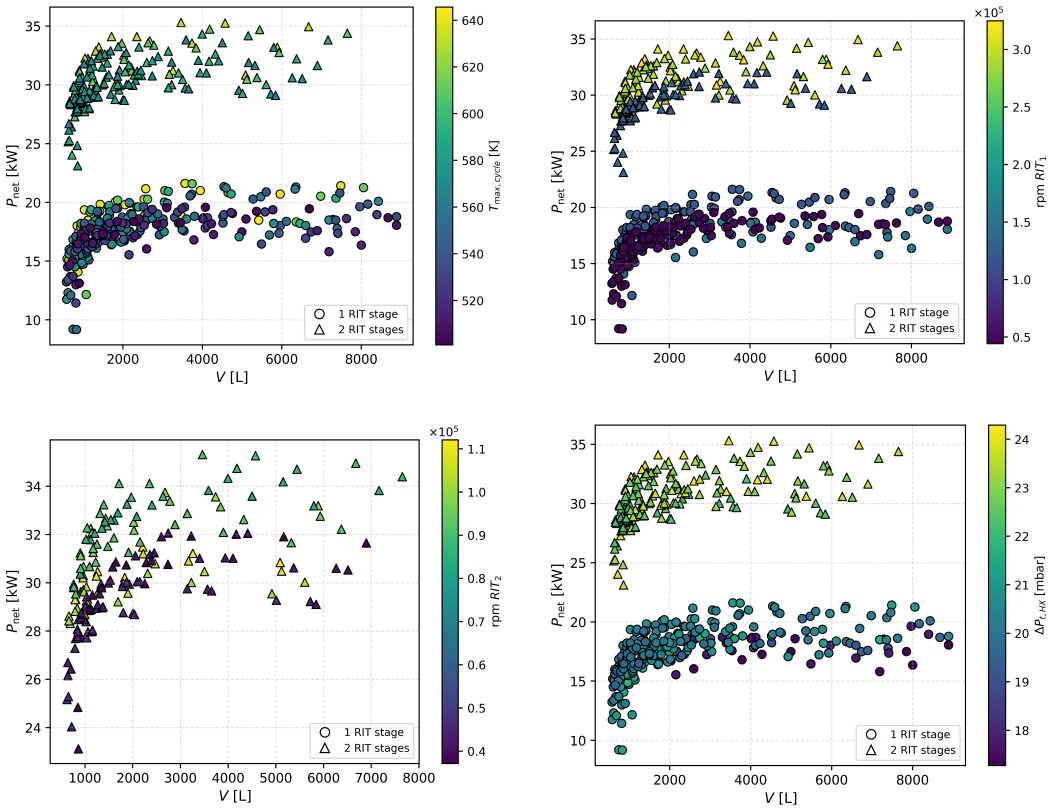


Figure 16. Net power output as a function of turbine volume for the feasible designs, colored by key operating parameters. From top left to bottom right: maximum cycle temperature T_{max}, rotational speed of the first RIT stage, rotational speed of the second RIT stage, and total pressure drop in the heat exchangers $\Delta P_{t,HX}$. Circular markers denote single-stage configurations, while triangular markers denote two-stage configurations.

4. Conclusions

This work presents an integrated modeling framework for the preliminary design and performance assessment of ORC-based waste heat recovery systems, with particular emphasis on the detailed representation of radial inflow turbines.

The main contributions of the modeling approach can be summarized as follows:

- Development of a quasi-one-dimensional RIT stage model capable of resolving multiple internal flow sections, enabling the prediction of both performance and geometry within a unified framework.
- Introduction of a dedicated formulation for shock-induced losses in the RIT stage, allowing for a more accurate description of supersonic flow conditions typical of high expansion ratio ORC turbines.
- Integration of models at the turbine, heat exchanger, and system levels within a computationally efficient environment suitable for large parametric studies.
- General applicability of the modeling framework with respect to both the type of working fluid and its thermodynamic state, allowing for analysis of ideal gas-like, dense vapor, and supercritical conditions within a unified formulation.
- Inclusion of practical design constraints such as thermal stability limits of the fluids, component sizes, and operating parameters such as rpm.

Application of the model to a WHR system coupled with a biofueled internal combustion engine led to the following main findings:

- A preliminary analysis of the main components highlighted the existence of optimal design regions arising from the tradeoffs between heat transfer performance, pressure losses, auxiliary consumption, and component sizing parameters.
- The coupling between the WHR system and the internal combustion engine, in particular the effect of the exhaust back-pressure, is of primary importance and cannot be neglected. Further dedicated analyses are required to fully quantify its impact.
- The existence of optimal operating conditions is consistently observed, resulting from the interplay between mass flow rate, expansion ratio, turbine efficiency, and components sizing parameters.
- Turbine performance exhibits an optimal pressure ratio, as the benefit of increasing expansion is progressively offset by efficiency degradation at high pressure ratios.
- The analysis of two-stage configurations highlights issues related to optimal stage balancing, which require further investigation and more detailed analysis.
- A clear tradeoff between system compactness and performance is identified, with diminishing returns in net power output beyond a certain increase in system volume.

Overall, the proposed framework demonstrates the ability to capture the key physical mechanisms governing ORC-based WHR systems, providing a reliable tool for preliminary design and supporting informed decisions on system architecture, working fluid selection, and operating conditions.

Future developments of the present framework include extension to off-design operating conditions, which is of primary importance for part-load performance assessment, as well as further improvements of the component models supported by high-fidelity CFD simulations. Although the present formulation has been generalized with respect to both the working fluid and the thermodynamic state such that the turbine model and shock-loss model are in principle applicable to fluids exhibiting non-classical gasdynamic behavior, e.g., BZT fluids, systematic verification under such conditions has not been carried out and represents a relevant direction for future work, as non-classical flow phenomena in the turbine passages may require dedicated modeling adaptations.

Author Contributions: Conceptualization, R.C., A.d.G., V.G. and F.R.; methodology, R.C. and F.R.; software, R.C.; writing—original draft preparation, R.C. and F.R.; writing—review and editing, R.C., A.d.G., V.G. and F.R.; supervision, F.R.; funding acquisition, F.R. All authors have read and agreed to the published version of the manuscript.

Funding: This work was funded by the Next Generation EU—Italian NRRP, Mission 4, Component 2, Investment 1.1 "Fund for the National Research Program and Projects of Significant National Interest (PRIN)" (Directorial Decree n. 1409/2022) "PRIN 2022 PNRR"—Title of the Project: Bio-FIRed IC Engines for off-grid Electric Vehicles ChaRging Stations (Bio-FiRE-for-EVer), Project Code: P2022K9T2S, CUP B53D23027060001. This work reflects only the authors' views and opinions, neither the Ministry for University and Research nor the European Commission can be considered responsible for them.

Data Availability Statement: The original contributions presented in this study are included in the article. Further inquiries can be directed to the corresponding author.

Conflicts of Interest: The authors declare no conflicts of interest.

Nomenclature

Abbreviations

ORC	Organic Rankine Cycle
WHR	Waste Heat Recovery
RIT	Radial Inflow Turbine
HX	Heat Exchanger
ICE	Internal Combustion Engine
TS	Total-to-Static
TT	Total-to-Total
DOE	Design of Experiments
VR	Volume Ratio
ODP	Ozone Depletion Potential
GWP	Global Warming Potential
BZT	Bethe–Zel'dovich–Thompson

Latin symbols

a	Speed of sound [m/s]
A	Area [m^2]
AR	Aspect ratio [-]
b	Passage width [m]
c	Flow velocity [m/s]
c_p, c_v	Specific heat capacities [J/kgK]
C_p	Heat capacity rate [W/K]
D	Diameter [m]
f	Friction factor [-]
G	Mass flux per unit area [kg/m^2s]
h	Specific enthalpy [J/kg]/convective heat transfer coefficient [W/m^2K]
H	Geometric term [-]
H_t	Total specific enthalpy [J/kg]
k	Thermal conductivity [W/mK]
l_z	Rotor axial length [m]
M	Mach number [-]
M_w	Molecular weight [g/mol]
MVR	Meridional velocity ratio [-]
$\dot{m}$	Mass flow rate [kg/s]
N_t	Number of tubes [-]
o	Blade opening [m]
p	Static pressure [Pa]

P	Power [W]
p_t	Total pressure [Pa]
Q	Vapor quality [-]
$\dot{Q}$	Heat transfer rate [W]
R	Gas constant [J/kgK]
Re	Reynolds number [-]
s	Specific entropy [J/kgK]
SP	Size parameter [m]
T	Temperature [K]
t_{te}	Trailing edge thickness [m]
u	Blade peripheral speed [m/s]
U	Overall heat transfer coefficient [W/m^{2}K]
V	Volume [m^3]
VR	Volumetric flow ratio [-]
X_r	Rotor diameter ratio [-]
X_v	Volute diameter ratio [-]
Z	Number of blades [-]/compressibility factor [-]
Greek symbols	
α	Absolute flow angle [deg]
β	Shock angle [deg]/pressure ratio [-]
γ	Specific heat ratio [-]
γ_{pv}	Isentropic pressure–volume exponent [-]
Γ	Fundamental derivative of gas dynamics [-]
δ	Flow deviation angle [deg]
Δ	Difference/increment
ε	Heat exchanger effectiveness [-]/tip clearance [m]
η	Efficiency [-]
θ	Relative flow angle [deg]
μ	Dynamic viscosity [Pa·s]
ν	Prandtl–Meyer function [deg]
ρ	Density [kg/m^3]
σ	Surface tension [N/m]/yield strength [MPa]
ϕ	Flow coefficient [-]/angular blade spacing [rad]
ψ	Work coefficient [-]
φ	Angular blade spacing [rad]
Subscripts	
0, 1, 2, 3, 4	Turbine flow stations
b	Blade/backplate
air	Air (condenser side)
amb	Ambient
bundle	Tube bundle
cond	Condenser
cr	Critical
cycle	Working fluid cycle
d	Downstream
dis	Discharge
exh	Exhaust gas
ext	External
fan	Fan
g	Nozzle throat/exit section
HX	Heat exchanger
in, out	Inlet/outlet
int	Internal
is	Isentropic

lim	Thermal stability limit
lm	Log-mean
m	Meridional component
max, min	Maximum/minimum
nb	Normal boiling point
net	Net value
n	Nozzle
pp	Pinch point
r	Rotor
s	Entropy-related/stage
SC	Subcooling
SE	Equivalent shock
t	Total quantity
te	Trailing edge
tip	Blade tip
ts	Total-to-static
tt	Total-to-total
u	Upstream
v	Volute
Superscripts	
$*$	Non-dimensional quantity
$'$, $''$	Modified reference state

References

1. Di Battista, D.; Fatigati, F.; Carapellucci, R.; Cipollone, R. An improvement to waste heat recovery in internal combustion engines via combined technologies. *Energy Convers. Manag.* **2021**, *232*, 113880. [CrossRef]
2. Firth, A.; Zhang, B.; Yang, A. Quantification of global waste heat and its environmental effects. *Appl. Energy* **2019**, *235*, 1314–1334. [CrossRef]
3. Wei, D.; Lu, X.; Lu, Z.; Gu, J. Performance analysis and optimization of organic Rankine cycle (ORC) for waste heat recovery. *Energy Convers. Manag.* **2007**, *48*, 1113–1119. [CrossRef]
4. Qiu, G. Selection of working fluids for micro-CHP systems with ORC. *Renew. Energy* **2012**, *48*, 565–570. [CrossRef]
5. Amicabile, S.; Lee, J.I.; Kum, D. A comprehensive design methodology of organic Rankine cycles for the waste heat recovery of automotive heavy-duty diesel engines. *Appl. Therm. Eng.* **2015**, *87*, 574–585. [CrossRef]
6. Lecompte, S.; Huisseune, H.; van den Broek, M.; Vanslambrouck, B.; De Paepe, M. Review of organic Rankine cycle (ORC) architectures for waste heat recovery. *Renew. Sustain. Energy Rev.* **2015**, *47*, 448–461. [CrossRef]
7. Patel, P.S.; Doyle, E.F. *Compounding the Truck Diesel Engine with an Organic Rankine-Cycle System*; Technical Report; SAE Technical Paper; SAE International: Warrendale, PA, USA, 1976.
8. Park, B.S.; Usman, M.; Imran, M.; Pesyridis, A. Review of Organic Rankine Cycle experimental data trends. *Energy Convers. Manag.* **2018**, *173*, 679–691. [CrossRef]
9. Liu, L.; Zhu, T.; Gao, N.; Gan, Z. A review of modeling approaches and tools for the off-design simulation of organic Rankine cycle. *J. Therm. Sci.* **2018**, *27*, 305–320. [CrossRef]
10. Moradi, R.; Cioccolanti, L. Modelling approaches of micro and small-scale organic Rankine cycle systems: A critical review. *Appl. Therm. Eng.* **2024**, *236*, 121505. [CrossRef]
11. Oh, J.; Jeong, H.; Kim, J.; Lee, H. Numerical and experimental investigation on thermal-hydraulic characteristics of a scroll expander for organic Rankine cycle. *Appl. Energy* **2020**, *278*, 115672. [CrossRef]
12. Wei, M.; Song, P.; Zhao, B.; Shi, L.; Wang, Z.; Ma, C. Unsteady flow in the suction process of a scroll expander for an ORC waste heat recovery system. *Appl. Therm. Eng.* **2015**, *78*, 460–470. [CrossRef]
13. He, Z.; Zhang, Y.; Dong, S.; Ma, H.; Yu, X.; Zhang, Y.; Ma, X.; Deng, N.; Sheng, Y. Thermodynamic analysis of a low-temperature organic Rankine cycle power plant operating at off-design conditions. *Appl. Therm. Eng.* **2017**, *113*, 937–951. [CrossRef]
14. Moradi, R.; Cioccolanti, L.; Del Zotto, L.; Renzi, M. Comparative sensitivity analysis of micro-scale gas turbine and supercritical CO_2 systems with bottoming organic Rankine cycles fed by the biomass gasification for decentralized trigeneration. *Energy* **2023**, *266*, 126491. [CrossRef]
15. Zhao, Y.; Liu, G.; Li, L.; Yang, Q.; Tang, B.; Liu, Y. Expansion devices for organic Rankine cycle (ORC) using in low temperature heat recovery: A review. *Energy Convers. Manag.* **2019**, *199*, 111944. [CrossRef]

16. Reale, F.; Calabria, R.; Massoli, P. Performance analysis of WHR systems for marine applications based on sCO_2 gas turbine and ORC. *Energies* **2023**, *16*, 4320. [CrossRef]
17. Manfredi, M.; Spinelli, A.; Astolfi, M. Definition of a general performance map for single stage radial inflow turbines and analysis of the impact of expander performance on the optimal ORC design in on-board waste heat recovery applications. *Appl. Therm. Eng.* **2023**, *224*, 119857. [CrossRef]
18. Wang, E.; Peng, N. A review on the preliminary design of axial and radial turbines for small-scale organic Rankine cycle. *Energies* **2023**, *16*, 3423. [CrossRef]
19. Li, C.; Guo, Z.; Guo, H.; Bao, X.; Zhou, L. Influences of main design parameters on the aerodynamic performance of a micro-radial inflow turbine. *AIP Adv.* **2022**, *12*, 105012. [CrossRef]
20. Meroni, A.; Robertson, M.; Martinez-Botas, R.; Haglind, F. A methodology for the preliminary design and performance prediction of high-pressure ratio radial-inflow turbines. *Energy* **2018**, *164*, 1062–1078. [CrossRef]
21. Whitfield, A.; Baines, N.C. *Design of Radial Turbomachines*; Longman Scientific & Technical: Harlow, UK; John Wiley & Sons, Inc.: New York, NY, USA, 1990.
22. Fiaschi, D.; Manfrida, G.; Maraschiello, F. Design and performance prediction of radial ORC turboexpanders. *Appl. Energy* **2015**, *138*, 517–532. [CrossRef]
23. Rodgers, C. *Mainline Performance Prediction for Radial Inflow Turbines*; Small High Pressure Ratio Turbines; SEE N 88-14364 06-37; Von Karman Institute for Fluid Dynamics: Sint-Genesius-Rode, Belgium, 1987; 29p.
24. Erbaş, M.; Bıyıkoğlu, A. Design and multi-objective optimization of organic Rankine turbine. *Int. J. Hydrogen Energy* **2015**, *40*, 15343–15351. [CrossRef]
25. Wasserbauer, C.A.; Glassman, A.J. *FORTRAN Program for Predicting Off-Design Performance of Radial-Inflow Turbines*; Technical Report; NASA: Washington, DC, USA, 1975.
26. Giovannelli, A.; Archilei, E.M.; Salvini, C. Two-stage radial turbine for a small waste heat recovery organic Rankine cycle (ORC) plant. *Energies* **2020**, *13*, 1054. [CrossRef]
27. Giglio, V.; di Gaeta, A.; Carandente, R.; Reale, F. Design and performance analysis of an 8.7-liter E100-fuelled SI engine integrated with an ORC waste heat recovery system for genset applications. *Energy Convers. Manag. X* **2026**, *30*, 101705. [CrossRef]
28. Sprouse, C., III; Depcik, C. Review of organic Rankine cycles for internal combustion engine exhaust waste heat recovery. *Appl. Therm. Eng.* **2013**, *51*, 711–722. [CrossRef]
29. Sprouse, C.E., III. Review of organic Rankine cycles for internal combustion engine waste heat recovery: Latest decade in review. *Sustainability* **2024**, *16*, 1924. [CrossRef]
30. Shi, L.; Shu, G.; Tian, H.; Deng, S. A review of modified Organic Rankine cycles (ORCs) for internal combustion engine waste heat recovery (ICE-WHR). *Renew. Sustain. Energy Rev.* **2018**, *92*, 95–110. [CrossRef]
31. Shu, G.; Li, X.; Tian, H.; Liang, X.; Wei, H.; Wang, X. Alkanes as working fluids for high-temperature exhaust heat recovery of diesel engine using organic Rankine cycle. *Appl. Energy* **2014**, *119*, 204–217. [CrossRef]
32. Lemmon, E.W.; Bell, I.H.; Huber, M.; McLinden, M. *NIST Standard Reference Database 23: Reference Fluid Thermodynamic and Transport Properties-REFPROP, Version 10.0*; Standard Reference Data Program, National Institute of Standards and Technology: Gaithersburg, MD, USA, 2018; pp. 45–46.
33. Kölsch, B.; Radulovic, J. Utilisation of diesel engine waste heat by Organic Rankine Cycle. *Appl. Therm. Eng.* **2015**, *78*, 437–448. [CrossRef]
34. Fatigati, F.; Coletta, A.; Di Bartolomeo, M.; Cipollone, R. The dynamic behaviour of ORC-based power units fed by exhaust gases of internal combustion engines in mobile applications. *Appl. Therm. Eng.* **2024**, *240*, 122215. [CrossRef]
35. Fatigati, F.; Di Battista, D.; Carapellucci, R. Model-based assessment of a feedforward-feedback control strategy for ORC-based unit in waste heat recovery application. *Appl. Therm. Eng.* **2025**, *258*, 124774. [CrossRef]
36. Wei, D.; Lu, X.; Lu, Z.; Gu, J. Dynamic modeling and simulation of an Organic Rankine Cycle (ORC) system for waste heat recovery. *Appl. Therm. Eng.* **2008**, *28*, 1216–1224. [CrossRef]
37. Bell, I.H.; Wronski, J.; Quoilin, S.; Lemort, V. Pure and Pseudo-pure Fluid Thermophysical Property Evaluation and the Open-Source Thermophysical Property Library CoolProp. *Ind. Eng. Chem. Res.* **2014**, *53*, 2498–2508. [CrossRef]
38. Baltadjiev, N.D.; Lettieri, C.; Spakovszky, Z.S. An Investigation of Real Gas Effects in Supercritical CO_2 Centrifugal Compressors. *J. Turbomach.* **2015**, *137*, 091003. [CrossRef]
39. Aungier, R.H. *Turbine Aerodynamics*; Concepts Eti: White River Junction, VT, USA, 2006; pp. 61–92.
40. Da Lio, L.; Manente, G.; Lazzaretto, A. A mean-line model to predict the design efficiency of radial inflow turbines in organic Rankine cycle (ORC) systems. *Appl. Energy* **2017**, *205*, 187–209. [CrossRef]
41. Benner, M.W.; Sjolander, S.; Moustapha, S. An empirical prediction method for secondary losses in turbines—Part II: A new secondary loss correlation. *J. Turbomach.* **2006**, *128*, 281–291. [CrossRef]
42. Denton, J. Loss Mechanisms in Turbomachines. *J. Turbomach.* **1993**, *115*, 621. [CrossRef]

43. Sieverding, C.H.; Stanislas, M.; Snoeck, J. The base pressure problem in transonic turbine cascades. *J. Eng. Power* **1980**, *102.3*, 711–718. [CrossRef]
44. Baumgärtner, D.; Otter, J.J.; Wheeler, A.P. The effect of isentropic exponent on transonic turbine performance. *J. Turbomach.* **2020**, *142*, 081007. [CrossRef]
45. Majer, M.; Pini, M. Design guidelines for high-pressure ratio supersonic radial-inflow turbines of organic Rankine cycle systems. *J. Glob. Power Propuls. Soc.* **2025**, *9*, 19–46. [CrossRef]
46. Baines, N. A meanline prediction method for radial turbine efficiency. In *Sixth International Conference on Turbocharging and Air Management Systems*; Institution of Mechanical Engineers: London, UK, 1998.
47. Moustapha H.; Zelesky M.F.; Baines, N.C.; Japiske, D. *Axial and Radial Turbines*; Concepts Eti: White River Junction, VT, USA, 2003.
48. Ventura, C.A.; Jacobs, P.A.; Rowlands, A.S.; Petrie-Repar, P.; Sauret, E. Preliminary design and performance estimation of radial inflow turbines: An automated approach. *J. Fluids Eng.* **2012**, *134*, 031102. [CrossRef]
49. Daily, J.W.; Nece, R.E. Chamber dimension effects on induced flow and frictional resistance of enclosed rotating disks. *J. Fluids Eng.* **1960**, *82*, 217–230. [CrossRef]
50. Ghosh, S.K.; Sahoo, R.; Sarangi, S.K. A computational approach to the design of a cryogenic turbine blade profile. *Int. J. Eng. Sci. Technol.* **2009**, *1*, 43–60. [CrossRef]
51. Zweifel, O. The spacing of turbo-machine blading, especially with large angular deflection. *Brown Boveri Rev.* **1945**, *32*, 436–444.
52. Glassman, A.J. *Computer Program for Design Analysis of Radial-Inflow Turbines*; Technical report; NASA Lewis Research Center: Cleveland, OH, USA, 1976.
53. Sieverding, C.; Manna, M. A review on turbine trailing edge flow. *Int. J. Turbomach. Propuls. Power* **2020**, *5*, 10. [CrossRef]
54. Bienner, A.; Gloerfelt, X.; Cinnella, P. Investigation of transonic flows through an idealized ORC turbine vane using Delayed Detached Eddy simulations. *Appl. Therm. Eng.* **2025**, *261*, 124951. [CrossRef]
55. Restrepo, J.C.; Bolaños-Acosta, A.F.; Simões-Moreira, J.R. Short nozzles design for real gas supersonic flow using the method of characteristics. *Appl. Therm. Eng.* **2022**, *207*, 118063. [CrossRef]
56. Cappiello, A.; Tuccillo, R. Design parameter influence on losses and downstream flow field uniformity in supersonic ORC radial-inflow turbine stators. *Int. J. Turbomach. Propuls. Power* **2021**, *6*, 38. [CrossRef]
57. Cramer, M.; Tarkenton, G. Transonic flows of Bethe—Zel'dovich—Thompson fluids. *J. Fluid Mech.* **1992**, *240*, 197–228. [CrossRef]
58. Thompson, P.A. A fundamental derivative in gasdynamics. *Phys. Fluids* **1971**, *14*, 1843–1849. [CrossRef]
59. Guardone, A.; Colonna, P.; Pini, M.; Spinelli, A. Nonideal compressible fluid dynamics of dense vapors and supercritical fluids. *Annu. Rev. Fluid Mech.* **2024**, *56*, 241–269. [CrossRef]
60. Medipati, C.; Chandrasekaran, N.; Falsetti, C.; Colonna, P. Rarefaction Shockwave Experiments in Dense Organic Vapours. In *Proceedings of the 5th International Seminar on Non-Ideal Compressible Fluid Dynamics for Propulsion and Power*; Springer: Berlin/Heidelberg, Germany, 2020, pp. 179–188.
61. Romei, A.; Vimercati, D.; Persico, G.; Guardone, A. Non-ideal compressible flows in supersonic turbine cascades. *J. Fluid Mech.* **2020**, *882*, A12. [CrossRef]
62. Cramer, M.; Crickenberger, A. Prandtl-Meyer function for dense gases. *AIAA J.* **1992**, *30*, 561–564. [CrossRef]
63. Benoit, H.; Spreafico, L.; Gauthier, D.; Flamant, G. Review of heat transfer fluids in tube-receivers used in concentrating solar thermal systems: Properties and heat transfer coefficients. *Renew. Sustain. Energy Rev.* **2016**, *55*, 298–315. [CrossRef]
64. Mahmoud, M.M.; Karayiannis, T.G. Heat transfer correlation for flow boiling in small to micro tubes. *Int. J. Heat Mass Transf.* **2013**, *66*, 553–574. [CrossRef]
65. Shah, M.M. Improved correlation for heat transfer during condensation in conventional and mini/micro channels. *Int. J. Refrig.* **2019**, *98*, 222–237. [CrossRef]
66. Haaland, S.E. Simple and explicit formulas for the friction factor in turbulent pipe flow. *J. Fluids Eng.* **1983**, *105*, 89–90. [CrossRef]
67. Ribatski, G.; Thome, J.R. Two-phase flow and heat transfer across horizontal tube bundles—A review. *Heat Transf. Eng.* **2007**, *28*, 508–524. [CrossRef]
68. Sung, T.; Yun, E.; Kim, H.D.; Yoon, S.Y.; Choi, B.S.; Kim, K.; Kim, J.; Jung, Y.B.; Kim, K.C. Performance characteristics of a 200-kW organic Rankine cycle system in a steel processing plant. *Appl. Energy* **2016**, *183*, 623–635. [CrossRef]
69. FPT Industrial. Cursor 9 NG Datasheet for Truck Applications. Available online: https://fptindustrial.aslabruna.it/en/motori/cursor-9-ng-221-kw/ (accessed on 16 January 2026).
70. Falbo, B.; Perrone, D.; Castiglione, T. Investigation on the Effects of Fuel Injection Systems on Evaporation for a Heavy-Duty Spark Ignition Ethanol Engine and Comparison with Methane. In Proceedings of the WCX SAE World Congress Experience, Detroit, MI, USA, 8 April 2025.
71. Krempus, D.; Bahamonde, S.; van der Stelt, T.P.; Klink, W.; Colonna, P.; De Servi, C.M. On mixtures as working fluids of air-cooled ORC bottoming power plants of gas turbines. *Appl. Therm. Eng.* **2024**, *236*, 121730. [CrossRef]
72. IPCC. *Climate Change 2021: The Physical Science Basis. Contribution of Working Group I to the Sixth Assessment Report of the Intergovernmental Panel on Climate Change*; Technical Report; Cambridge University Press: Cambridge, UK; New York, NY, USA, 2021. [CrossRef]

73. *ANSI/ASHRAE Standard 34-2022*: Designation and Safety Classification of Refrigerants. American Society of Heating, Refrigerating and Air-Conditioning Engineers: Atlanta, GA, USA, 2022.
74. Liu, X.; Lim, H.-S.; Choi, B.-S.; Myint, A.A.; Kim, J. Thermal decomposition characteristics of the refrigerant R1234ze(E). *J. Therm. Sci.* **2023**, *32*, 104602.
75. Mota-Babiloni, A.; Navarro-Esbrí, J.; Molés, F.; Cervera, ÁB.; Peris, B.; Verdú, G. A review of refrigerant R1234ze(E) recent investigations. *Appl. Therm. Eng.* **2016**, *95*, 211–222. [CrossRef]
76. Dixon, S.L.; Hall, C.A. *Fluid Mechanics and Thermodynamics of Turbomachinery*, 7th ed.; Butterworth-Heinemann: Oxford, UK, 2014.
77. Futral, S.M.; Holeski, D.E. *Experimental Investigation of Radial Inflow Turbine Performance with Tip Clearance Effects*; Technical Report NASA TN D-XXXX; NASA: Washington, DC, USA, 1970.
78. Spence, S.W.T.; Artt, D.W. Experimental performance evaluation of a radial inflow turbine. *Proc. Inst. Mech. Eng. Part A J. Power Energy* **2007**, *221*, 611–620.
79. Sieverding, C.H. Recent progress in the understanding of basic aspects of secondary flows in turbine blade passages. *J. Eng. Gas Turbines Power* **1985**, *107*, 248–257. [CrossRef]
80. Cappiello, A.; Majer, M.; Tuccillo, R.; Pini, M. On the influence of stator-rotor radial gap size on the fluid-dynamic performance of mini-ORC supersonic turbines. In *Turbo Expo: Power for Land, Sea, and Air*; American Society of Mechanical Engineers: New York, NY, USA, 2022; Volume 86106, p. V10BT35A015.

Disclaimer/Publisher's Note: The statements, opinions and data contained in all publications are solely those of the individual author(s) and contributor(s) and not of MDPI and/or the editor(s). MDPI and/or the editor(s) disclaim responsibility for any injury to people or property resulting from any ideas, methods, instructions or products referred to in the content.